

A resolved warm/dense gas Schmidt-Kennicutt relationship in a binary HyLIRG at $z = 2.41$

ALMA observations of H-ATLAS J084933.4+021443

Jonathan S. Gómez^{1,2}, Hugo Messias³, Neil M. Nagar¹ Gustavo Orellana^{1,4}, R. J. Ivison^{5,6}, and Paul van der Werf⁷

¹ Astronomy Department, Universidad de Concepción, Concepción, Chile
e-mail: jonathangomez@udec.cl

² Departamento Astronomía y Astrofísica, Pontificia Universidad Católica de Chile, Av. Vicuña Mackenna 4860, Stgo., Chile

³ Joint ALMA Observatory, Alonso de Córdova 3107, Vitacura 763-0355, Santiago, Chile

⁴ Instituto de Física y Astronomía, Universidad de Valparaíso, Avda. Gran Bretaña 1111, Valparaíso, Chile

⁵ European Southern Observatory, Karl-Schwarzschild-Straße-2, 85748 Garching bei München, Germany

⁶ Institute for Astronomy, University of Edinburgh, Royal Observatory, Blackford Hill, Edinburgh EH9 3HJ, UK

⁷ Leiden Observatory, Leiden University, P.O. Box 9513, NL-2300 RA Leiden, The Netherlands

Received June 5, 2018; accepted XXX 2018

Submitted to Astronomy & Astrophysics

ABSTRACT

Aims. Hyperluminous infrared galaxies (HyLIRGs; star-formation rates of up to $\approx 1000 M_{\odot} \text{ yr}^{-1}$) – while rare – provide crucial ‘long lever arm’ constraints on galaxy evolution. HATLAS J084933.4+021443, a $z = 2.41$ binary HyLIRG with at least two additional luminous companion galaxies, is thus an optimal test-ground for studies of star formation and galaxy evolution during ‘cosmic noon’.

Methods. We have used ALMA to obtain *resolved* imaging and kinematics of atomic and molecular emission lines, and rest-frame 340- to 1160 GHz continuum emission, for the known luminous component galaxies in H-ATLAS J084933.4+021443: W, T, M, C.

Results. All four component galaxies are spatially (~ 0.3 or 2.5 kpc) resolved in CO J:7–6, [C I] 2–1, H₂O and the millimetre (mm) to sub-mm continuum. Rotation-dominated gas kinematics is confirmed in W and T. The significant extension to component T, in gas and continuum, along its kinematic minor axis, is attributable to its lensing magnification. Spatially resolved sub-mm spectral energy distributions (SEDs) reveal that component W is well fit with greybody emission from dust at a single temperature over the full extent of the galaxy, despite it containing a powerful AGN, while component T requires an additional component of hotter nuclear dust and additional sources of emission in the mm. We confirm that [C I] 2–1 can be used as a rough tracer of warm/dense molecular gas in extreme systems, though the [C I] 2–1/CO luminosity ratio increases sub-linearly. We obtain an exquisite and unprecedented resolved (2.5-kpc-scale) ‘warm/dense molecular gas’ Schmidt-Kennicutt (SK) relationship for components W and T. Gas exhaustion times for all apertures in W (T) are 1–4 Gyr (0.5–2 Gyr). Both W and T follow a resolved ‘warm/dense gas’ SK relationship with power law $n \sim 1.7$, significantly steeper than the $n \sim 1$ found previously via ‘cold’ molecular gas in nearby ‘normal’ star-forming galaxies.

Key words. Galaxies: formation – galaxies: high-redshift – infrared: galaxies – infrared: jets and outflows – radio continuum: galaxies – submillimeter: galaxies

1. Introduction

Sub-millimetre surveys have greatly advanced our understanding of galaxy evolution by uncovering a population of heavily dust-obscured galaxies at high redshift, the so-called sub-millimetre galaxies (SMGs). Although the first of these to be discovered (Ivison et al. 1998) was a hyperluminous infrared (IR) galaxy (HyLIRG; $L_{\text{IR}} \geq 10^{13} L_{\odot}$, where the IR luminosity is measured across $\lambda_{\text{rest}} = 8\text{--}1000 \mu\text{m}$), the vast majority of the numerous SMGs uncovered thereafter were ultraluminous infrared galaxies (ULIRGs; $L_{\text{IR}} \geq 10^{12} L_{\odot}$, forming stars at $\geq 100 M_{\odot} \text{ yr}^{-1}$ – see, e.g., Blain et al. 2002; Casey et al. 2014; Fudamoto et al. 2017). The importance of SMGs in studies of galaxy formation and evolution has been underlined by *Spitzer* and *Herschel Space Observatory* results which show that SMGs contribute significantly to the total amount of star formation in the early Universe (e.g. Magnelli et al. (2009); Glenn et al. (2010)).

The IR luminosity of a HyLIRG implies an extreme star-formation rate (Kennicutt 1998), $\text{SFR} \geq 10^3 M_{\odot} \text{ yr}^{-1}$, in the ab-

sence of a significant contribution to L_{IR} from an active galactic nucleus (AGN) and for a ‘normal’ (Chabrier 2003) stellar initial mass function (IMF), although Zhang et al. (2018) showed recently that the IMF in dusty starbursts must be top heavy. Naively, this suggests starburst lifetimes of only ~ 100 Myr, unless star formation migrates around an extended gas reservoir. While rare and extreme, HyLIRGs are excellent laboratories with which to confront the most recent hydrodynamic simulations (Bahé et al. 2017; Barnes et al. 2017; Benoit et al. 2017; Suková et al. 2017; Schartmann et al. 2017; Lagos et al. 2018) of isolated and merging galaxies (e.g. Hayward et al. (2011)), test star-formation ‘laws’, and the effect of feedback, driven by AGN (e.g. Bouché et al. (2010); Davé et al. (2011, 2012); Ciccone et al. (2014)) and/or intense star formation (e.g., Shetty & Ostriker (2012); Lilly et al. (2013)) on the evolution of a galaxy.

Of specific relevance to the results presented here are the resolved Schmidt-Kennicutt (SK) relationship (Schmidt 1959; Kennicutt 1989), i.e. the power-law relationship between the

surface density of gas and star formation ($\Sigma_{\text{SFR}} \propto \Sigma_{\text{H}_2}^N$) on \leq kpc scales within a galaxy, and the use of the sub-mm C I lines instead of CO (Flower & Launay 1985; Downes & Solomon 1998; Yang et al. 2010; Bolatto et al. 2013; Carilli & Walter 2013; Rodríguez et al. 2014) or HCN (Gao 1997; Gao & Solomon 2004; Shimajiri et al. 2017; Oteo et al. 2017) to estimate the total molecular gas of a galaxy (Walter et al. 2011; Israel et al. 2015; Qian Jiao et al. 2017). While the galaxy-integrated SK relation, i.e. the surface densities of the galaxy-integrated star formation and cold molecular gas mass (hereafter the galaxy-integrated SK relationship), has been extensively studied – e.g. Young et al. (1986), Solomon & Sage (1988), Buat et al. (1989), Gao & Solomon (2004), Bouché et al. (2007), Krumholz & Thompson (2007), Daddi et al. (2010), Genzel et al. (2010), Kennicutt & Evans (2012), Chelsea et al. (2016) – the resolved SK relationship (at \leq 1-kpc resolution within galaxies; hereafter kpc-scale SK) has been constrained in relatively few nearby (Wong & Blitz 2002; Kennicutt et al. 2007; Bigiel et al. 2008; Leroy et al. 2008; Krumholz et al. 2009; Bigiel et al. 2010, 2011; Boquien et al. 2011; Momose et al. 2013; Roychowdhury et al. 2015) and high-redshift (Freundlich et al. 2013; Thomson et al. 2015) galaxies. Bigiel et al. (2008) and Bigiel et al. (2011) find that 1 kpc-scale resolved SK relationship in their ‘normal’ star-forming galaxies is consistent with an exponent of $N \sim 1$. In contrast, Momose et al. (2013) find a super-linear slope ($N = 1.3$, and even up to 1.8) for the resolved SK relationship in their sample of nearby spirals. A super-linear slope ($N = 1.5$) was also found by Roychowdhury et al. (2015) in H I-dominated regions of nearby spiral and dwarf galaxies.

The $[\text{C I}]^3 P_2 \rightarrow^3 P_1$ and $[\text{C I}]^3 P_1 \rightarrow^3 P_0$ lines – both are required to determine the excitation temperature of C I (Stutzki et al. 1997) – can be used to robustly determine the mass of the neutral carbon (Stutzki et al. 1997; Weiß et al. 2003, 2005). In ultraviolet (UV) or cosmic ray-dominated regions, the (typically optically thin) C I emission lines are expected to be primarily produced in the dissociated surfaces of molecular clouds, though observations show that they are present throughout the cloud (e.g. Glover et al. 2015) and have been argued to be a better tracer of total molecular gas mass than the CO line (Weiß et al. 2003, 2005; Bisbas et al. 2015; Glover & Clark 2016). Our detections of both CO and $[\text{C I}]^2-1$ (even if only the higher of the two C I sub-mm lines) in four independent galaxies (spatially resolved in two) allow us to compare both species as molecular gas tracers. Molecular lines from e.g. H_2O , HCN and CS have a much higher critical density and therefore probe the dense molecular star-forming phase. Omont et al. (2013) find a relation between the far-infrared (FIR) and H_2O luminosities for a sample of high-redshift starburst galaxies. The H_2O detections for this sample are all associated with underlying FIR emission, implying that the H_2O emission traces star-forming regions. However, the H_2O molecules can also be excited in the dissipation of supersonic turbulence in molecular gas or by slow shocks (e.g. Flower & Pineau 2010). In the case of purely shock-excited H_2O , it is unlikely that underlying FIR emission would be detected in regions of strong H_2O emission (e.g. Goicoechea et al. 2015; Anderl et al. 2013).

The HyLIRG, HATLAS J084933.4+021443 (hereafter HATLAS J084933) at $z = 2.41$, though identified only in 2012, is now one of the few well-studied HyLIRGs (Ivison et al. (2013); hereafter I13). It has a relatively brief literature history: identified in the *Herschel* ATLAS imaging survey (Eales et al. 2010) as a 350 μm peaker, then CO J:1–0 spectroscopy with the Greenbank Telescope (GBT) constrained its redshift to 2.410 (Harris et al. 2012). I13 presented a detailed study of the molecular gas

and rest-frame sub-mm emission of this source using the Jansky Very Large Array (CO J:1–0), CARMA (CO J:3–2), IRAM PdBI (CO J:4–3) together with continuum imaging from the SMA, *Herschel*, *Spitzer*, VISTA, and *HST*, and optical spectroscopy from Keck. They determined that HATLAS J084933 comprises at least four starburst galaxies scattered across a ~ 100 -kpc region at $z = 2.41$. The two brightest galaxies, dubbed W and T, both HyLIRGs in their own right, are separated by ~ 85 kpc on the sky. Of these, T is amplified modestly by a foreground galaxy with a lensing magnification of $\sim 2\times$. The molecular gas reservoirs of W and T, each ~ 3 kpc in size, are rotation-dominated, and counter-rotate. These two components have CO line strengths and widths typical of the brightest SMGs and lie among SMGs in the ‘global’ (i.e. galaxy-wide) equivalent of the Schmidt-Kennicutt relationship. Two other components, dubbed M and C, are ULIRGs, though they lie relatively close to the HyLIRG cutoff. Their estimated molecular gas masses (but not their estimated dynamical masses) are almost a factor $10\times$ lower than those of W and T.

With the goal of a more comprehensive study of the physics in HATLAS J084933 – particularly with the goal of probing the resolved Schmidt-Kennicutt relationship at the highest SFRs and gas densities – but also of exploring the resolved kinematics (rotation vs. dispersion), and searching for evidence of outflows via kinematics and P Cygni profiles (e.g. molecular outflows as seen by Ciccone et al. 2014, Feruglio et al. 2010), we have obtained new observations using the Atacama Large millimetre/sub-millimetre Array (ALMA) of this source. These new observations include resolved imaging of the CO J:3–2 and CO J:7–6 emission lines (tracers of the dense molecular gas), the $[\text{C I}]^3 P_2 \rightarrow^3 P_1$ fine-structure line ($\nu_{\text{rest}} = 809.34$ GHz; hereafter $[\text{C I}]^2-1$), and the H_2O 2₁₁ – 2₀₂ emission line ($\nu_{\text{rest}} = 752.03$ GHz, hereafter H_2O). These lines are detected and resolved towards all four principal components of HATLAS J084933: W, T, C, and M, thus allowing a significant improvement in our understanding of the source as compared to I13. We additionally obtained resolved continuum imaging at rest-frame 341 GHz, 750 GHz, 808 GHz, and 1160 GHz, which can be used as a tracer of the resolved star-formation rate and dust mass, amongst other quantities.

In this work we present the first set of results based on the new ALMA data. A forthcoming paper will address the resolved dust properties and the resolved (atomic and molecular) gas to dust ratios. In Section 2 we detail our ALMA sub-mm observations. The results of these observations are presented in Section 3. In Section 4 we analyse and discuss the results and present our conclusions. We adopt a cosmology with $H_0 = 71$ km s⁻¹ Mpc⁻¹, $\Omega_m = 0.27$, and $\Omega_\Lambda = 0.73$, so 1'' is equivalent to 8.25 kpc at $z = 2.41$.

2. Observations and Data Processing

HATLAS J084933 was observed by ALMA as part of Project 2012.1.00463.S (P.I.: G. Orellana) during ALMA Cycle 2. Four of the five approved ‘science goals’ of the project were observed over the period 2015 August to September, as detailed below. The fifth science goal, designed to observe the CO J:9–8 line (of both ¹²CO and ¹³CO) plus nearby water vapour and OH+ lines, was not observed.

We used the Common Astronomy Software Applications (CASA 4.4.0) software for all data calibration and imaging steps, thus obtaining the final data cubes, continuum maps, emission-line only cubes, and moment 0, 1, and 2 maps of the individual

emission lines. Further processing and analysis was performed with our Interactive Data Language (IDL) and Python codes.

2.1. CO J:3–2 and rest-frame 341 GHz (880 μm) continuum imaging

Approximately 35 min of on-source integration was obtained in Band 3 with thirty four 12-meter during 2015 August 30. The Band 6 receivers were to the CO J:3–2 line ($\nu_{rest} = 345.795991$ GHz (Morton & Noreau 1994), redshifted to $\nu_{obs} = 101.465$ GHz) in one of the four spectral windows (SPWs). The second SPW in the upper sideband (USB) was set to partially cover the CS J:7–6 line and the two SPWs in the lower sideband (LSB) did not cover any known strong lines and were thus intended to detect continuum emission. To maximise sensitivity, the ALMA correlator was used in ‘continuum’ or Time Division Multiplexing (TDM) mode, which gave a spacing of ~ 46 km s $^{-1}$ per channel and a total velocity coverage of ~ 5000 km s $^{-1}$ per baseband.

Using a Briggs weighting with a robust parameter of +0.5, and the intrinsic spectral resolution, the CO line was imaged with a synthesised (FWHM) beam of $1''.13 \times 0''.51$ with a position angle (P.A.) of 115° . The r.m.s. noise was $\sigma = 0.27$ mJy beam $^{-1}$ in each 46 km s $^{-1}$ channel. Line-free channels were used to create a continuum map at observed-frame ~ 100 GHz (rest-frame ~ 341 GHz); here the synthesised beam was $1''.23 \times 0''.56$ beam FWHM (P.A., 116°) and the r.m.s. noise was $\sigma = 0.08$ mJy beam $^{-1}$.

2.2. CO J:7–6, [C I] $^3P_2 \rightarrow ^3P_1$, and rest-frame 808 GHz (370 μm) continuum imaging

Approximately 21 min of on-source integration time was obtained in Band 6 with thirty four 12-meter antennas in 2015 September. The last scan of the observation was not on the phase-calibrator, but rather on the target. Nevertheless, the target is bright enough to enable self-calibration, hence making that scan usable. Two overlapping spectral windows in the USB were tuned to contiguously cover both the CO J:7–6 line ($\nu_{rest} = 806.651801$ GHz; Morton & Noreau (1994), redshifted to an observed frequency of ~ 236 GHz), and the [C I] $^3P_2 \rightarrow ^3P_1$ ([C I] 2–1) line ($\nu_{rest} = 809.34197$ GHz; Müller et al. (2001), redshifted to an observed frequency of ~ 237 GHz). The other two spectral windows were set to cover a water vapour line and neighbouring continuum (see next subsection). Once more, for maximum sensitivity, the correlator was set to TDM mode resulting in a spectral spacing of 19.7 km s $^{-1}$ per channel and a total velocity coverage of ~ 2500 km s $^{-1}$ per SPW for all SPWs.

Image cubes of the CO J:7–6 and [C I] 2–1 line were made at the intrinsic spectral resolution (19.7 km s $^{-1}$ channels) and using natural weighting, resulting in a synthesised (FWHM) beam of $0''.27 \times 0''.24$ at P.A., 3.9° . The r.m.s. noise in each channel was 0.31 mJy beam $^{-1}$ for the CO J:7–6 and [C I] 2–1 line cubes. Line-free channels were used to make a map of the continuum emission near observed frequency 237 GHz (corresponding to rest frequency 808 GHz). Here, maps made with Briggs robust parameter of +0.5 resulted in a synthesised beam of $0''.26 \times 0''.24$ at P.A., 2.9° and an r.m.s. noise of $\sigma = 0.24$ mJy beam $^{-1}$.

2.3. H₂O 2₁₁ – 2₀₂ Imaging, and 750 GHz (400 μm) continuum imaging

In the science goal described in the previous Section (in which the USB was used to cover the CO J:7–6 and [C I] 2–1 line), the two LSB SPWs were set to 220.538 GHz, the redshifted frequency of the H₂O 2₁₁ – 2₀₂ (H₂O) line ($\nu_{rest} = 752.033143$ GHz; Dionne et al. (1980)), and the neighbouring continuum. The spectral spacing was 21.2 km s $^{-1}$ per channel. The image cube of the H₂O 2₁₁ – 2₀₂ line, made with natural weighting, had an r.m.s. noise of 0.34 mJy beam $^{-1}$ per native channel and a synthesised (FWHM) beam size of $0''.29 \times 0''.26$ at P.A., 13.7° . Line-free channels in these two LSB SPWs were used to make a map of the continuum emission near observed frequency, 220 GHz (corresponding to rest-frame frequency, 750 GHz). Here, maps made with Briggs robust parameter of +0.5 resulted in a synthesised beam of $0''.28 \times 0''.26$ at P.A., 179° and an r.m.s. noise of $\sigma = 0.17$ $\mu\text{Jy beam}^{-1}$.

2.4. Observed frame 340 GHz (rest-frame 1160 GHz or 260 μm) Continuum Imaging

Approximately 53 min of on-source integration was obtained with 38 working 12-meter antennas during 2015 June 5. The spectral set-up was designed to detect four different water vapour lines, one in each SPW, none of which were detected. This dataset was thus used only to obtain a continuum image near observed-frame 340 GHz (corresponding to rest frame 1160 GHz). The receivers were tuned such that the USB was centred at 1160 GHz (260 μm). A weighting scheme with Briggs robust parameter of +0.5 resulted in a synthesised beam of $0''.34 \times 0''.3$ (P.A., 83.6°) and a noise level of $\sigma = 0.26$ mJy beam $^{-1}$ in the continuum image.

3. Results

Continuum emission at all observed frequencies is strongly detected and resolved towards galaxy components W and T and relatively weakly detected in components C and M. The emission lines CO J:3–2, CO J:7–6, and [C I] 2–1 are also strongly detected and resolved in W and T and weakly (but reliably) detected and resolved in components C and M. Further, the H₂O line is detected, and spatially resolved, in components W and T. No other emission lines or components (i.e. galaxies) were reliably detected in our continuum or line imaging.

In the following subsections, we first present galaxy-integrated measurements (both continuum and emission line) for each of the four components, then the resolved continuum and emission line maps, the resolved galaxy kinematics, and finally other galaxy resolved quantities including resolved emission line ratios and a resolved ‘warm/dense gas’ Schmidt-Kennicutt relationship.

3.1. Galaxy-integrated properties: line profiles and ratios, continuum emission, and other measured quantities

The emission lines of CO J:3–2, CO J:7–6, [C I] $^3P_2 \rightarrow ^3P_1$ and H₂O 2₁₁–2₀₂ are detected in the four previously identified galaxies of the HATLAS J084933 system (W, T, M and C); of these, the latter has the weakest lines. The observed galaxy-integrated spectra of CO J:7–6 and [C I] 2–1 in components W and T are shown in Fig. 1. Unfortunately, the relatively close rest frequencies of CO J:7–6 and [C I] 2–1 (rest-frame $\Delta\nu = 2.7$ GHz or $\Delta v = 1050$ km s $^{-1}$) and the relatively broad velocity profile of the

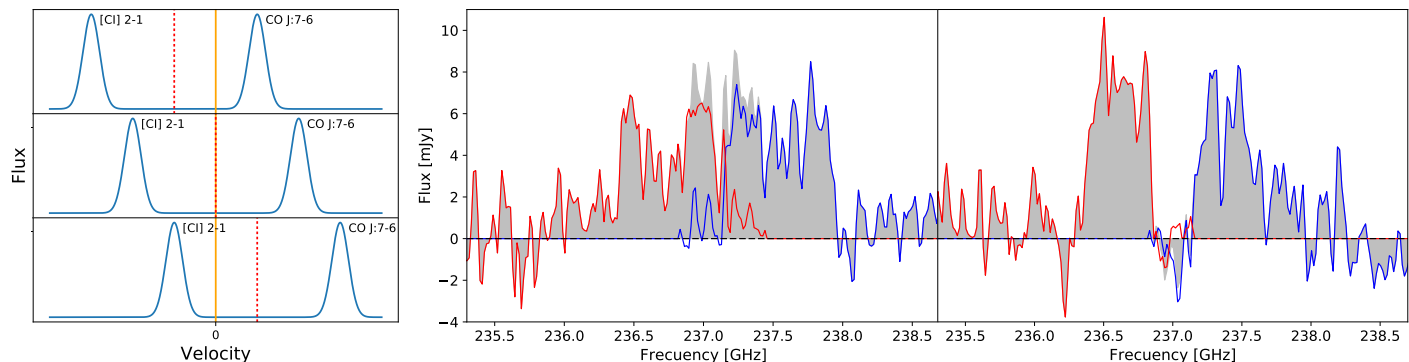


Fig. 1. Left panel: an illustration of the method used to separate the CO J:7–6 and [C I] 2–1 lines in individual channels of the datacube (see text). The dashed red line shows our choice for the dividing frequency (based on the fitted gas rotation model) and the solid yellow line shows the systemic velocity of the galaxy (see Section 3.1). Middle and right panels: the observed (grey filled regions) and rotation-model-separated profiles (see text) of the CO J:7–6 (red) and [C I] 2–1 (blue) emission lines in component W (middle panel) and component T (right panel).

lines in component W results in a super-position of these two lines in the galaxy-integrated spectra of W; a similar (albeit less blended) situation is also seen in component T (see Fig. 1).

Given that CO J:7–6 and [C I] 2–1 show relatively similar ordered velocity fields, and our argument that these velocity fields are best interpreted as rotation (see Section 3.4), we are able to separate the emission from the two lines. That is, the two lines can be cleanly separated in individual (19.7 km s^{-1}) velocity channels of our data cube: the width of each line is $\sim 100\text{--}250 \text{ km s}^{-1}$ in a given velocity channel while the separation between the lines is $\sim 1000 \text{ km s}^{-1}$. This clear separation between the two lines in individual velocity channels was visually verified in the data cube. We thus use our rotation-only velocity models (see Section 3.4) to predict, for each spatial pixel, the velocity (or channel) which would most cleanly separate the CO J:7–6 and [C I] 2–1 lines. The left panel of Fig. 1 illustrates our choice of the dividing frequency (dashed red line) for a given systemic ruled by the rotation of the galaxy, blue- or red-shifted spatial pixel of the galaxy. The rotation-model-separated profiles are shown with blue and red lines in the middle and right panels of Fig. 1 for components W and T, respectively. Note that this separation is valid only if all the gas participates in rotation; a weak outflow component with velocities $\geq 500 \text{ km s}^{-1}$ may not be validly separated by our method.

The galaxy-integrated profiles of all detected emission lines in W and T are shown in the right-most panels of Figs 7 and 8, respectively, and those corresponding to components C and M (where de-blending was not necessary) are shown in the right-most panels of Fig. 9.

A direct comparison of the galaxy integrated line profiles of CO J:7–6 and [C I] 2–1 in components W and T are shown in Fig. 2. In W, both profiles show a double-horned structure, either a result of the global galaxy kinematics or attributable to higher optical depths at velocities closer to systemic. Additionally, while the redshifted emission from the two lines are relatively well matched (in a normalised sense), the CO J:7–6 emission shows a significant excess over [C I] 2–1 at blue-shifted velocities. Both of the above points, at a less significant level, could also be claimed to be true in component T. In component T we also call attention to the potential absorption feature at $\sim 400 \text{ km s}^{-1}$ seen in both species; this is discussed in more detail in Section 3.5.

Galaxy-integrated (for each component W, T, C and M) measurements of the continuum flux densities, emission-line fluxes

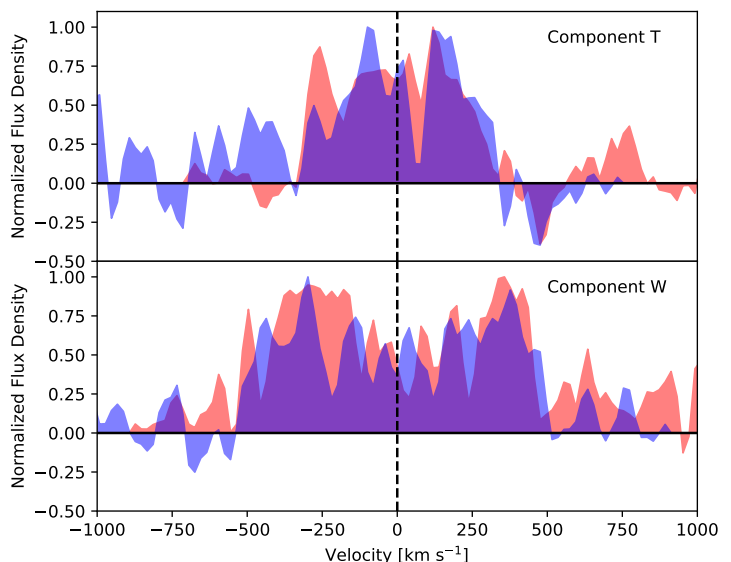


Fig. 2. A comparison of the galaxy-integrated normalized spectral profiles of the CO J:7–6 (red) and [C I] 2–1 (light blue) lines for component T (top panel) and W (bottom panel). Overlap regions of the two spectra appear darker blue. The dashed black line shows our adopted zero velocity.

and luminosities, dynamical mass estimates and molecular gas masses, obtained from our new dataset, are listed in Table 1. For easy reference, the estimated dust temperature and the total IR luminosity obtained from detailed global SED modelling by I13 are also listed in the table. The quantities listed in Table 1 were derived as follows: the dynamical mass is calculated under the assumption that the galaxy velocity field is rotation-dominated (see Section 3.4): $M_{\text{dyn}} = [R \times (v_{\text{max}} / \sin(i))^2] / G = [R \times V_{\text{asym}}^2] / G$, where G is the gravitational constant, v_{max} is the maximum projected rotational velocity, i is the galaxy disk inclination, V_{asym} is the asymptotic inclination-corrected rotational velocity listed in Tables 4 and 5, and R was taken to be the deconvolved half-light radius in CO J:3–2.

Table 1. HATLAS J084933.4+021443: line fluxes and luminosities, observed continuum fluxes, and derived properties

Property	unit of measurement	W	T	C	M
$S_{\text{CO}J:3--2}$	[Jy km s ⁻¹]	4.29±0.53	4.22±0.46	0.95±0.28	0.63±0.16
$S_{\text{CO}J:7--6}$	[Jy km s ⁻¹]	2.704±0.73	2.72±0.51	0.51±0.36	0.46±0.27
$S_{[\text{C}i]2-1}$	[Jy km s ⁻¹]	2.07±0.82	1.33±0.86	0.21±0.19	-
$S_{\text{H}_2\text{O}}$	[Jy km s ⁻¹]	0.69±0.23	0.87±0.09	-	-
$L'_{\text{CO}J:3--2}$	[10 ⁹ K km s ⁻¹ pc ²]	134±10	133±10	29.9±8.7	19.8±4.9
$L'_{\text{CO}J:7--6}$	[10 ⁹ K km s ⁻¹ pc ²]	15.5±2.2	15.6±1.4	2.93±2.0	2.64±1.5
$L'_{[\text{C}i]2-1}$	[10 ⁹ K km s ⁻¹ pc ²]	11.8±2.6	7.6±1.9	1.2±1.0	-
$L'_{\text{H}_2\text{O}}$	[10 ⁹ K km s ⁻¹ pc ²]	4.58±2.2	5.77±1.4	-	-
$S_{\text{vobs}100\text{GHz}}$	[mJy]	0.18 ±0.08	0.11±0.08	-	-
$S_{\text{vobs}220\text{GHz}}$	[mJy]	5.14 ±0.17	3.63±0.17	0.41±0.17	0.36±0.17
$S_{\text{vobs}237\text{GHz}}$	[mJy]	5.79 ±0.24	4.39±0.24	0.38±0.24	0.51±0.24
$S_{\text{vobs}340\text{GHz}}$	[mJy]	22.9 ±0.26	21.4±0.55	2.59±0.55	1.8±0.5
$\log M_{\text{dyn}}$	[M_{\odot}]	11.86±0.7	11.51±0.9	10.55±0.13	10.22±0.16
($T_{\text{ex}}=30$ K): $\log M_{\text{C}i}$	[M_{\odot}]	8.41	8.22	7.42	-
($T_{\text{ex}}=40$ K): $\log M_{\text{C}i}$	[M_{\odot}]	8.28	8.1	7.29	-
$\log M_{\text{H}_2}$ (from C I; $T_{\text{ex}}=40$ K)	[M_{\odot}]	12.0	11.8	11.0	-
T_{dust}^a	[K]	39.8±1.0	36.2±1.1	-	-
$\log L_{\text{IR}}^a$	[L_{\odot}]	13.52±0.04	13.16±0.05	12.9±0.2	12.8±0.2
$\log M_{\text{H}_2+\text{He}}^a$ (from CO)	[M_{\odot}]	11.04±0.12	11.10±0.13	10.25±0.15	10.11±0.14

^a : from Ivison et al. (2013).

Emission-line luminosities (L'_{CO} ; in units of in K km s⁻¹ pc²) are calculated using:

$$L'_{\text{CO}} = 3.25 \times 10^7 \times S_{\text{CO}} \Delta \nu \frac{D_L^2}{(1+z)^3 \nu_{\text{obs}}^2} \quad (1)$$

where $S_{\text{CO}} \Delta \nu$ is the measured flux of the emission line in Jy km s⁻¹, D_L is the luminosity distance in Mpc, z is the redshift, and ν_{obs} is the observed frequency of the line in GHz (Solomon, Downes & Radford 1992).

The molecular gas mass is typically estimated from the CO J:1–0 (hereafter CO) luminosity (Solomon & Vanden Bout 2005) using

$$M_{\text{mol}} = \alpha_{\text{CO}} \times L'_{\text{CO}} \quad (2)$$

where M_{mol} has units of M_{\odot} and α_{CO} has units of $M_{\odot}/(\text{K km s}^{-1} \text{ pc}^2)$. There remains significant debate on the value of α_{CO} . While for nearby ‘normal’ star-forming galaxies a value of $\alpha_{\text{CO}} \sim 4.3 M_{\odot} (\text{K km s}^{-1} \text{ pc}^2)^{-1}$ is recommended (Bolatto et al. 2013), the value of α_{CO} is often lower in starburst galaxies. In a seminal analysis of CO radiative transfer and gas dynamics in the starburst nuclei of low-redshift ULIRGs on scales < 1 kpc, Downes & Solomon (1998) found a characteristic value of the conversion factor for H₂ + He of $\alpha_{\text{CO}} \sim 0.8 M_{\odot} (\text{K km s}^{-1} \text{ pc}^2)^{-1}$ in these systems. This value, which implies more CO emission per unit molecular gas mass, is commonly adopted for IR-luminous starbursts, where the gas is not in virialised individual clouds (Bolatto et al. 2013). Given the extreme starburst nature of the four components of HATLAS J084933.4+021443, and for consistency with I13, we use $\alpha_{\text{CO}} \sim 0.8$ in this work, while noting that a higher value may be more appropriate. In Table 1 we list the galaxy-integrated molecular gas mass obtained using the CO J:1–0 luminosity of I13. In future sections we use our resolved CO J:7–6 maps, together with the global CO J:7–6 to CO J:1–0 ratios for each component, to obtain resolved molecular gas masses within each component.

The neutral carbon gas mass has been estimated following Weiß et al. (2003), assuming that the [C I] 2–1 line is optically

thin. Since we have only observed the [C I] 2–1 line (and not the [C I] $^3P_1 \rightarrow ^3P_0$ line) we must assume an excitation temperature (T_{ex}) for C I. When both C I lines have been observed, the derived T_{ex} is $\leq T_{\text{dust}}$ (Stutzki et al. 1997; Weiß et al. 2005; Popping et al. 2017). Table 1 thus lists the estimated [C I] 2–1 masses for two assumed values of T_{ex} which bracket the estimated dust temperatures (I13) of components W and T. As mentioned in Section 1 the [C I] 2–1 mass has been used to trace the total molecular gas mass, and this estimate is likely to be more reliable than that via CO in low-metallicity galaxies and in environments with strong UV or cosmic ray dissociation (Bisbas et al. 2015). The conversion of [C I] 2–1 gas mass to total molecular gas mass is still under debate and here we follow Weiß et al. (2003) in using $X_{[\text{C}i]} = M_{[\text{C}i]}/(6M_{\text{H}_2}) = 3 \times 10^{-5}$; note that this assumes an adopted carbon abundance 50% higher than the Galactic abundance. Note also that the molecular gas masses estimated from [C I] 2–1 in Table 1 are derived from the [C I] 2–1 gas masses calculated assuming $T_{\text{ex}} = 40$ K.

The variation of the galaxy-integrated CO line luminosity with CO rotational transition (the ‘CO ladder’) for each of the four components of HATLAS J084933.4+021443 is shown in Fig. 3. Component W appears to peak at CO J:3–2, while T, C, and M are roughly flat between CO J:3–2 and CO J:4–3. Note that the CO J:4–3 data of I13 come from observations with IRAM PdBI (6 antennas) in its most extended configuration: the relatively limited uv spacing as compared to our ALMA CO J:3–2 observation could mean that the former images missed some line emission. Thus, conservatively, we can only claim that the CO ladder peaks somewhere between CO J:3–2 and CO J:6–5 for all four components. A peak at J~5 in these galaxies would be consistent with the CO ladders seen in typical SMGs (Carilli & Walter 2013). Note that the uncertainty in the location of the peak of the CO ladder does not cause additional uncertainties in our conversion between CO J:7–6 and CO J:1–0 luminosities in later sections.

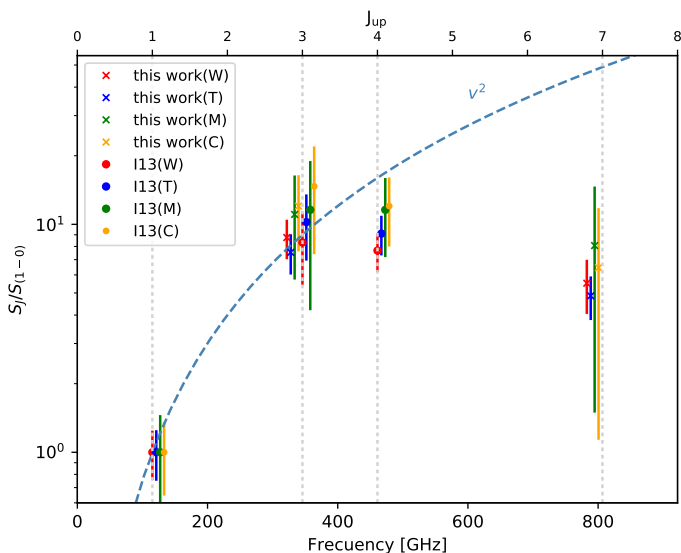


Fig. 3. The CO ladder for all (four) components of HATLAS J084933.4+021443: W (red), T (blue), M (purple), and C (light green). The x -axis is labelled with the rotational quantum number of the upper state (top; 1, 3, 4, and 7; small displacements in the x -axis are used for the different points to avoid confusion) and the rest frequency of the line (bottom) and the y -axis is the line flux normalised to that of CO J:1–0. Line fluxes from this work are shown with solid circles and those from I13 are shown with diamonds. The dashed line shows the CO ladder expectation for the case of a constant brightness temperature on the Rayleigh-Jeans (RJ) scale, i.e. $S \sim \nu^2$ (note that the RJ approximation is not valid for high J).

3.2. Resolved Continuum: Maps and Spectral Shape

Continuum emission at all observed frequencies, corresponding to rest-frame frequencies of 341 GHz (880 μm), 750 GHz (400 μm), 808 GHz (370 μm) and 1160 GHz (260 μm) at $z = 2.41$, is strongly detected and resolved towards galaxy components W and T and relatively weakly detected in components C and M. Of the four frequencies, the observed 340 GHz (corresponding to rest-frame 1160 GHz or 260 μm) continuum maps yielded both the highest resolution and the highest signal-to-noise detections; these are shown in Fig. 6. Interestingly, the continuum emission of component T is primarily extended along its kinematic minor axis (thin white line in the panel), though at the faintest emission levels it is also extended along the major axis especially to the SE. The brighter continuum emission in component W appears extended along PA $\sim 100^\circ$, an angle between the major and minor kinematic axes; at these brighter continuum emission levels W does not show any clear extension along its kinematic major axis. Only when considering the fainter continuum emission is W more extended along its major axis. Component C shows a potential extension in PA $\sim 105^\circ$: to the W as a connected extension and to the E as a lower significance separated knot. The distribution of the continuum emission in W and T along the major and minor kinematic axes can also be appreciated in Fig. 5, where these are compared to the emission line flux distributions.

In the following subsections, we use the observed-frame 340 GHz maps (rest frame 260 μm emission) to constrain the global and resolved star formation rates of each component.

We explore the resolved continuum spectral slopes of components W and T by comparing the four observed continuum lu-

minosities in multiple resolved apertures (Fig. 4). To obtain the data in each panel, the higher resolution image was convolved with a Gaussian to degrade the resolution to that of the lower-resolution image. The data in the figure were then extracted over apertures with sizes equivalent to the FWHM of the synthesised beam of the lower resolution image, with half a beam spacing between apertures. Thus roughly a quarter of the data points are independent. I13 fitted the observed galaxy-wide sub-mm SEDs of W and T with a model of greybody (assuming emissivity, $\beta = 2.0$) emission from dust at a single temperature, obtaining dust temperatures of 39.8 ± 0.1 K and 36.1 ± 1.1 K for W and T, respectively. The predictions of greybody emission with these temperatures and $\beta = 2.0$ are plotted in all panels of Fig. 4. Between 370 and 400 μm (middle panel of Fig. 4) the resolved dust temperatures are roughly in agreement with the globally-derived values, though the nuclear apertures of both W and T (the highest luminosities) have flux density ratios which imply dust temperatures higher by several tens of degrees. Both at longer wavelengths (880 μm ; left panel of Fig. 4) and at the shortest observed wavelengths, which are closest to the IR peak (260 μm ; right panel of Fig. 4), component W continues to follow the global temperature predictions. Component T, however, shows significant excess emission at both the longest and shortest wavelengths: all apertures of T show a consistent flux excess at 880 μm (left panel) attributable to cooler dust temperatures or an additional source of 880 μm emission; the nuclear apertures of T show a consistent excess of 260 μm emission implying significantly higher temperatures for a single dust component or the presence of a second hotter component of dust. Both excesses could be explained by the presence of an AGN: the nuclear dust would be heated by the AGN, leading to the short-wavelength excess, and synchrotron and thermal emission from a powerful AGN jet could explain the excess emission seen at mm wavelengths.

The relationship between the resolved continuum spectral slopes (and thus dust mass and temperature) and the atomic and molecular gas emission (and thus mass and excitation), is deferred to a future work.

3.3. Component Sizes and Emission-Line Maps

All detected emission lines – CO J:3–2, CO J:7–6, [C I] 2–1 and H₂O – are resolved across several synthesised beams in W and T, and the CO J:7–6 and [C I] 2–1 lines are partially resolved in C and M. Components W and T show the largest spatial extents in both continuum and line emission. Comparisons of the spatial distribution of the CO J:7–6, [C I] 2–1, and rest-frame 1160 GHz continuum emission along two position angles (PAs) on the sky in components W and T are shown in Fig. 5. These PAs represent the major and minor kinematic axes under the assumption that the kinematics in W and T are rotation-dominated (Section 3.4).

Within the noise, the distributions of the gas and continuum emission are roughly similar in component W, though there is some indication that the gas (especially [C I] 2–1) emission is more extended than the continuum emission along the kinematic minor axis. Additionally, and unexpectedly, the emission from both atomic and molecular gas is more extended along the minor axis, rather than the major axis. Even more significant differences are seen in component T. Here too the gas and dust is more extended along the minor instead of the major axis. Along the minor axis there are significant offsets between the locations of the peak CO J:7–6, [C I] 2–1 and continuum emission. The continuum peak (the ‘SW knot’) has a significantly higher CO to [C I] 2–1 ratio as compared to the NE extension; similar to

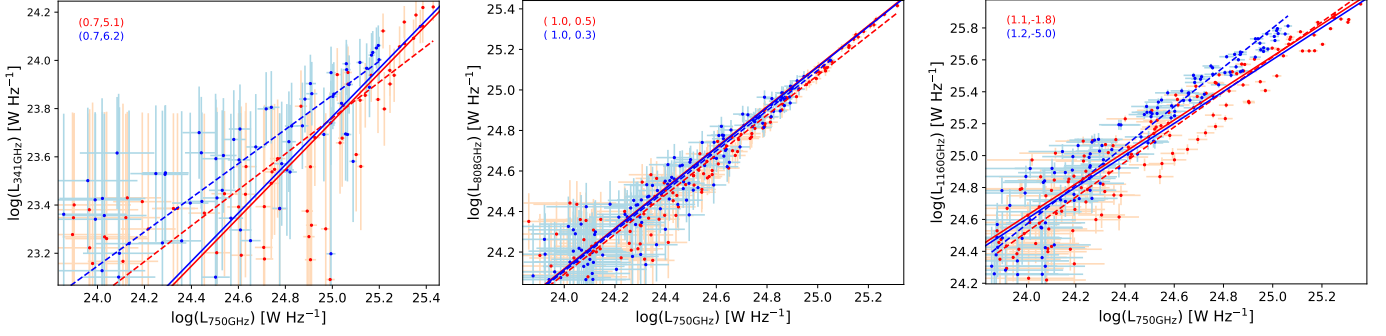


Fig. 4. The relationships between the (resolved) continuum luminosities at rest-frame 341 GHz (880 μm), 750 GHz (400 μm), 808 GHz (370 μm), and 1160 GHz (260 μm) for components W (red points) and T (blue points). The two maps used for each panel were convolved to a common resolution. Each data point was calculated over an aperture equivalent to the FWHM of the synthesised beam, with apertures spaced by half a synthesised beam; i.e. roughly a quarter of the data points are independent measurements. Error bars for each point are shown in light red and light blue for component W and T, respectively. The dashed lines in the corresponding colour delineate the linear fits to the data; the coefficients of these fits (slope, intercept) are listed in the panel in the corresponding colour. The solid lines show the expected relationships for greybody emission (with $\beta = 2.0$) for dust at temperature, $T_{\text{dust}} = 40$ K (red) and 36 K (blue), the estimated dust temperatures derived by I13 for W and T, respectively.

[C I] 2–1, the H₂O emission is also stronger in the NE extension as compared to the SW knot (see the next Section). The continuum-to-gas ratios are highest in the NE extension and lowest in the SW knot. Along the kinematic major axis, the gas and continuum are relatively similarly distributed, except for a [C I] 2–1-rich region 0''.4 from the nucleus. The deconvolved sizes of components W and T along the PAs shown in Fig. 5 are listed in Tables 2 and 3.

Table 2. Observed-frame 340-GHz continuum sizes

Component	kinematic minor-axis	kinematic major-axis
W	0.46''(3.80 kpc)	0.45''(3.71 kpc)
T	0.75''(6.19 kpc)	0.39''(3.22 kpc)

Table 3. CO J:7–6 size

Component	kinematic minor-axis	kinematic major-axis
W	0.58''(4.79 kpc)	0.53''(4.37 kpc)
T	0.75''(6.19 kpc)	0.36''(2.97 kpc)

The moment maps (0 = integrated flux, 1 = intensity weighted velocity map, 2 = velocity dispersion map) of the CO J:3–2, CO J:7–6, [C I] 2–1 and H₂O emission lines are presented in Figs 7, 8, and 9, for components, W, T, and C and M, respectively. The galaxy-integrated line profiles shown in the right-most column of these figures were extracted from the square apertures shown in the left-most column (moment 0) maps: a 3''x3'' aperture centred on RA +2°14' 44''.618 DEC 8^h 49^m 33^s.592 for all lines in W, a 3''x3'' aperture centred on RA +2°14' 39''.697 DEC 8^h 49^m 32^s.960 for all lines in T. The CO J:3–2 line profile of C and M together are extracted over a 3''.8x3''.8 aperture centred on RA +2°14' 45''.219 DEC 8^h 49^m 33^s.868. The individual CO J:7–6 line profiles of C and M have been extracted over a 0''.5x0''.5 aperture centred on each component.

All four components show ordered velocity fields. In W and T, both CO and [C I] 2–1 show consistent blue- and red-shifted sides and similar peak-to-peak velocities. The molecular gas velocity fields are best appreciated in the CO J:7–6 (rather than CO

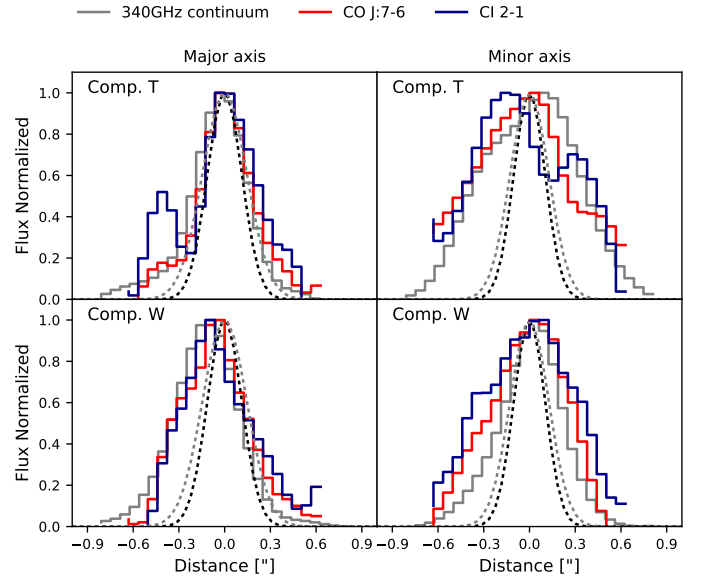


Fig. 5. The spatial extent of the emission line gas (CO J:7–6 and [C I] 2–1) and rest-frame 1160-GHz continuum emission in component T (top row) and component W (bottom row) along the kinematic major (PA=135° for T and PA=55° for W) and kinematic minor axes (PA=225° for T and PA=145° for W). These major and minor axes are illustrated in Figs 6, 7 and 8. Each panel shows the normalised flux, extracted along a one-pixel-wide slit oriented along the corresponding PA, of the continuum emission (grey solid line; obtained from the observed 340-GHz continuum map), the CO J:7–6 emission line (dark red solid line) and the [C I] 2–1 emission line (dark blue solid line). The major axis of the synthesised beam of the CO J:7–6 and [C I] 2–1 moment 0 maps (340-GHz continuum map) is shown by the grey (black) normalised Gaussian. Both synthesised beams are close to circular. Both lines and continuum are clearly resolved in all panels, with similar extensions in both emission lines and the continuum. The deconvolved sizes along these PAs are listed in Tables 2 and 3.

J:3–2) velocity maps which have both the highest signal to noise and the highest spatial resolution. Components W and T show (projected) maximum velocities of roughly ± 500 km s⁻¹ and ± 270 km s⁻¹, respectively. Components M and C have smaller velocity gradients, with $v_{\text{max}} = 132$ km s⁻¹ (264 km s⁻¹ peak to

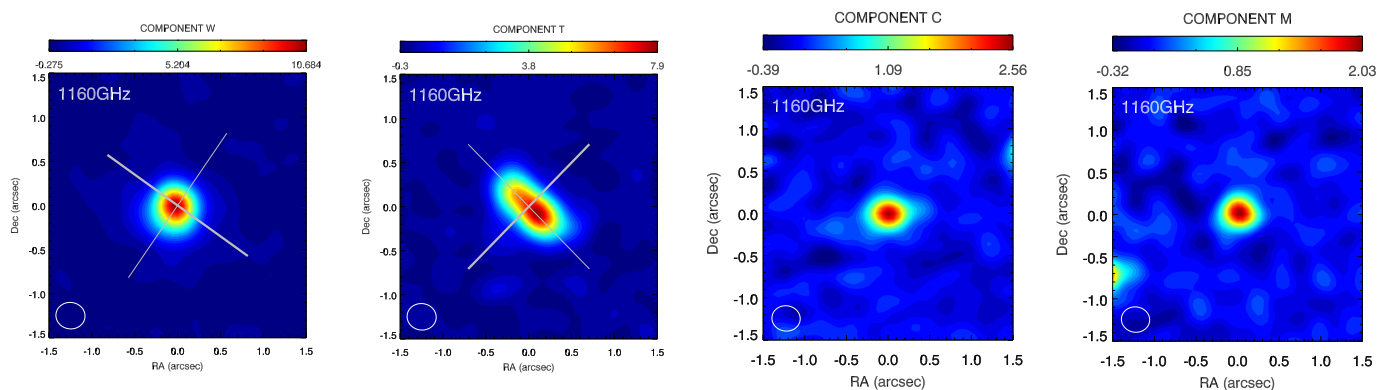


Fig. 6. Maps of the observed-frame 340-GHz (corresponding to rest-frame $260\ \mu\text{m}$) continuum emission in (left to right) components W, T, C and M. Continuum fluxes are in mJy beam^{-1} following the colour bar above each panel. Each panel is $3'' \times 3''$ in size and the axes, in arcsec, are centred on the kinematic centre of each component, as obtained from *Kinometry*. These kinematic nuclear positions, hereafter used as the galaxy positions, are: W: 08:49:33.6XX, +02:14:44.68; T: 08:49:33.0XX, +02:14:39.69; C: 08:49:33.9XX, +02:14:44.86; M: 08:49:33.8XX, +02:14:45.58. For components W and T, the kinematic major and minor axes are shown with thick and thin grey lines, respectively.

peak) and $v_{max} = 164\ \text{km s}^{-1}$ ($327\ \text{km s}^{-1}$ peak to peak), respectively. Note that the internal kinematics of components C and M are resolved for the first time in our CO J:7–6 and [C I] 2–1 maps. Further, the relatively low spatial resolution CO J:3–2 maps show an almost continuous (in flux and velocity) bridge between C and M. The CO and [C I] 2–1 dispersion maps show higher dispersions near the nucleus, and along the kinematic minor axis; the former can be partly due to the rotational velocity gradient along the major axis. The observed velocity fields could be interpreted as either ordered rotation (Section 3.4 or outflows in a galaxy disk (Section 3.5); in the following section we argue for the former scenario.

The H_2O emission line, which admittedly has a lower signal to noise, appears to follow different kinematics as compared to CO and [C I] 2–1. In W, the blue and redshifted components of H_2O can be argued to be separated by the kinematic minor axis (i.e. the same as CO) or the kinematic major axis. In T the kinematics is significantly more disordered, with blue shifted velocities seen along the kinematic major axis on both sides of the kinematic minor axis, and an isolated red velocity component at the edge of the detected extent.

While the CO and [C I] 2–1 lines follow roughly similar kinematics in W, there are notable differences in both their morphology and kinematics: e.g. CO J:7–6 shows a notable blueshifted highly-dispersive NE-clump which is not present in [C I] 2–1. These differences are the primary reason for the different global emission line profiles presented in the previous section.

In component T, the CO and [C I] 2–1 emission lines show relatively similar kinematics. While CO J:7–6 emission is roughly centred on the ‘nucleus’ the [C I] 2–1 and water vapour line emission straddle the nucleus, similar to what is seen in the (rest-frame) 1160 GHz continuum emission. Note that component T (see the CO J:7–6 maps) is highly extended along its kinematic minor axis (see middle panel of Fig. 8); this was not obvious in the earlier I13 maps due to their lower resolution. The extension along the minor axis is best appreciated in Fig. 5 and Tables 2, and 3. If the velocity field in T is interpreted as due to rotation, then the ratio of the minor/major axes in this galaxy implies that the lensing-produced spatial magnification of this component is $\geq 2\times$ along the direction of the minor axis.

Both C and M are also resolved kinematically in the CO J:7–6 line (Fig. 9) and also in the [C I] 2–1 line (not shown): if their velocity fields are due to rotating gas, then the major axis PAs of

C and M are $\sim -30^\circ$, and $\sim 160^\circ$, respectively. The lower resolution CO J:3–2 maps appear to show a continuous bridge, in integrated flux and in velocity, between the two components. Given their small spatial and velocity separation, it is likely that these two components are interacting, which is known to be common amongst SMGs (e.g. Ivison et al. 2007; Engel et al. 2010).

The galaxy-integrated CO and [C I] 2–1 emission line profiles in W and T can be interpreted as double-peaked or as having a central plateau. This spectral shape could be due to the intrinsic velocity distribution of gas, due to the emission lines being optically thick, or even due to the presence of superposed absorption line components which originate in outflowing atomic and molecular gas.

3.4. Modelling the Observed Velocities: Rotation

Table 4. Results of *Kinometry* modelling of component W

Property	CO J:3–2	CO J:7–6	[C I] $^3P_2 \rightarrow ^3P_1$
PA.	45°	55°	55°
Inclination	48°	48°	48°
V_{asym} (km s^{-1})	464	525	525

Rows are (a) PA (N to E); (b) inclination (0° is face-on); and (c) V_{asym} , the peak to peak de-projected rotation velocity.

Table 5. Results of *Kinometry* modelling of Component T

Property	CO J:3–2	CO J:7–6	[C I] $^3P_2 \rightarrow ^3P_1$
PA.	144°	136°	135°
Inclination	49°	54°	49°
V_{asym} (km s^{-1})	298	241	298

Rows are as in Table 4.

As mentioned in the previous section, the ordered velocity fields in W and T could be interpreted as either rotation or outflows within the disk. The rotation scenario – the more likely one – is supported by the pattern seen in the position-velocity diagrams presented in Section 3.5. The velocity fields of all strongly detected emission lines in components W and T were input to the *Kinometry* package (Krajinović et al. 2006) in order to constrain the kinematic centre, position angle of the line of nodes, and

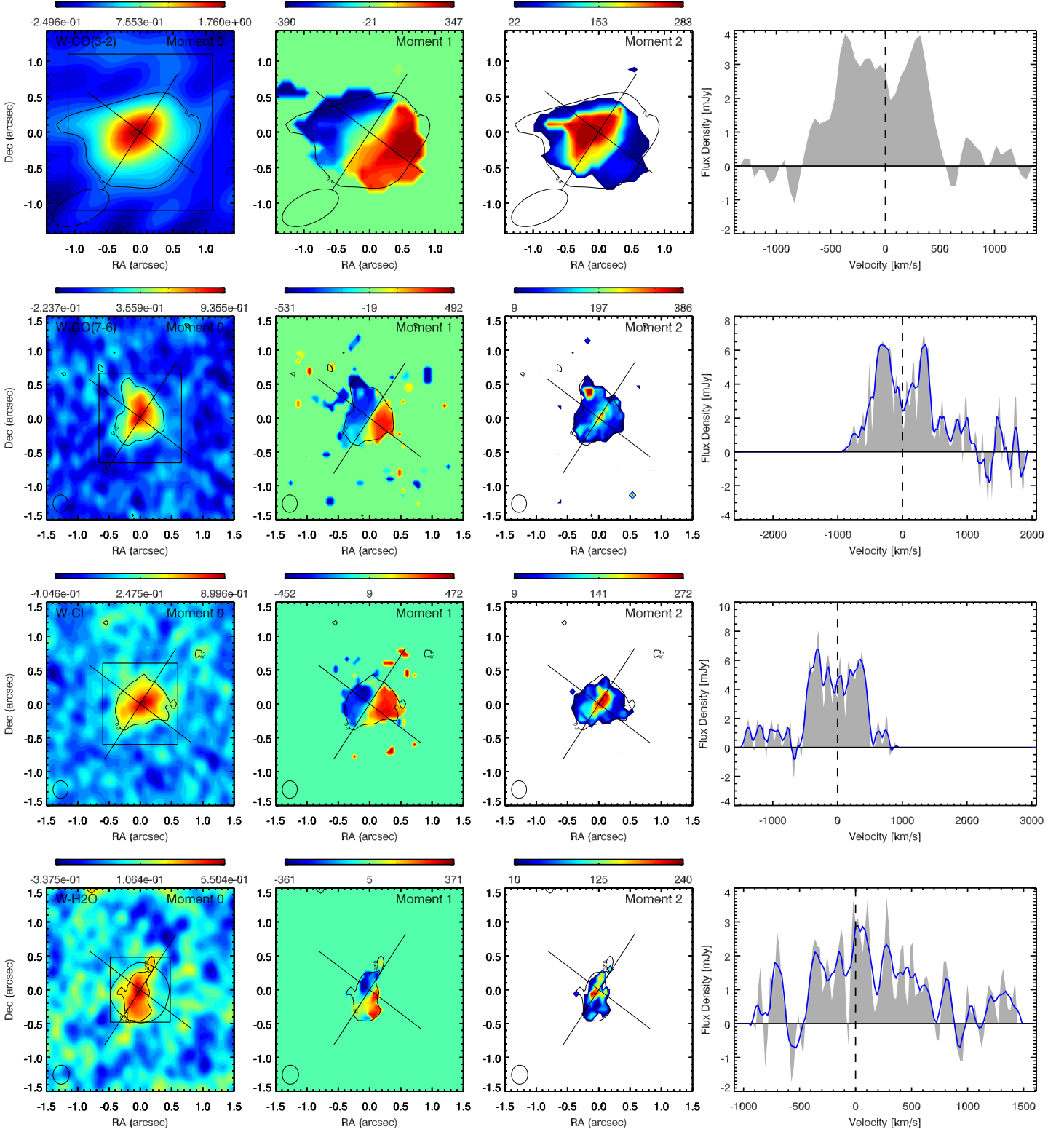


Fig. 7. For component W, we show from left to right: maps of the integrated flux (moment 0; units of $\text{Jy km s}^{-1} \text{beam}^{-1}$), intensity-weighted average velocity (moment 1; km s^{-1} relative to systemic), and velocity dispersion (moment 2; km s^{-1}), and the galaxy-integrated line profile, of the emission lines detected. From top to bottom the lines are: CO J:3–2, CO J:7–6, $[\text{C I}]^3 P_2 \rightarrow ^3 P_1$ and $\text{H}_2\text{O } 2_{11} - 2_{02}$. In the three left-most columns the colours follow the respective colour bars, the synthesised beam is shown at the lower left, and axes units are arcseconds with the same central position used in all panels. For ease, the kinematic major and minor axes are shown in black solid lines and an illustrative single flux contour from the moment 0 image is shown in all panels of the same row. All moment maps were made from data cubes created with natural weighting. The right-most column shows the corresponding galaxy-integrated line profile extracted within the square apertures shown in the corresponding left-most panel (i.e. the moment 0 image). The line profiles are shown both at the observed spectral resolution (grey histograms; spectral resolutions of – top to bottom – 46 km s^{-1} , 19.7 km s^{-1} , 19.7 km s^{-1} , and 21.2 km s^{-1} , per channel), and at a smoothed resolution (blue solid lines in the lower three panels) of $\sim 100 \text{ km s}^{-1}$. The line profiles of CO J:7–6 and $[\text{C I}]^3 P_2 \rightarrow ^3 P_1$ have been de-blended as explained in Section 3.1.

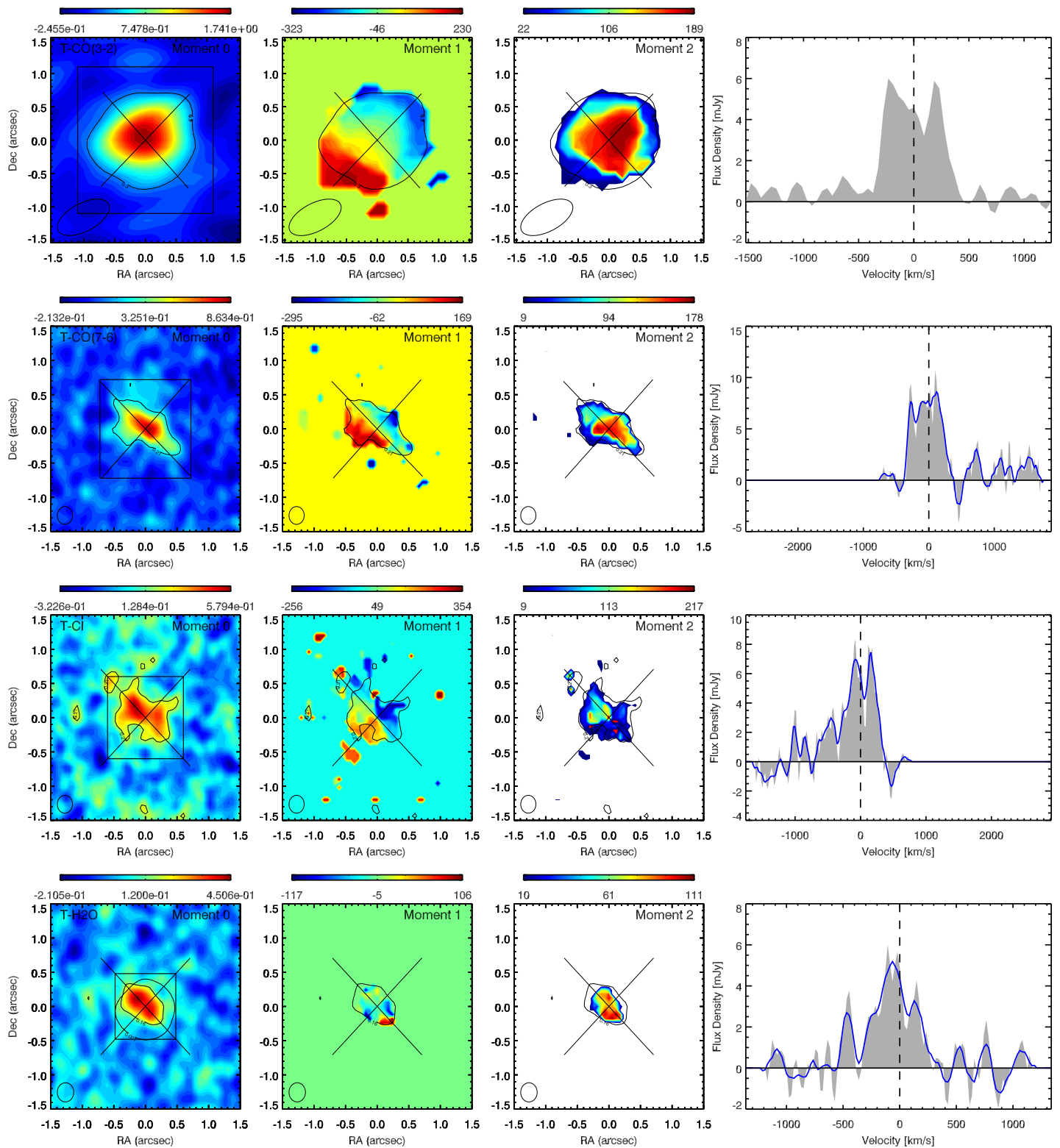


Fig. 8. As in Fig. 7 but for component T. Here the relatively narrow line profiles, as compared to W, allow a cleaner separation of the galaxy-wide CO J:7–6 and [C I] $^3P_2 \rightarrow ^3P_1$ line profiles.

the inclination, and the rotation curve of the galaxy, all under the assumption that the velocity field is rotation-dominated. The initial guess for the nuclear position was that of the rest-frame 1160-GHz continuum peak. The resulting parameters obtained by *Kinemetry* are listed in Tables 4 and 5, and in the caption of Fig. 6. Note that in the tables, V_{asym} is the asymptotic inclination-

corrected rotational velocity. Clearly within each component the *Kinemetry*-determined PA and inclination are similar for CO J:3–2, CO J:7–6, and [C I] 2–1, though the results from the CO J:3–2 line are significantly different, most likely due to their significantly lower spatial resolution. We created a simple toy rotation model for each of W and T. This rotation model follows

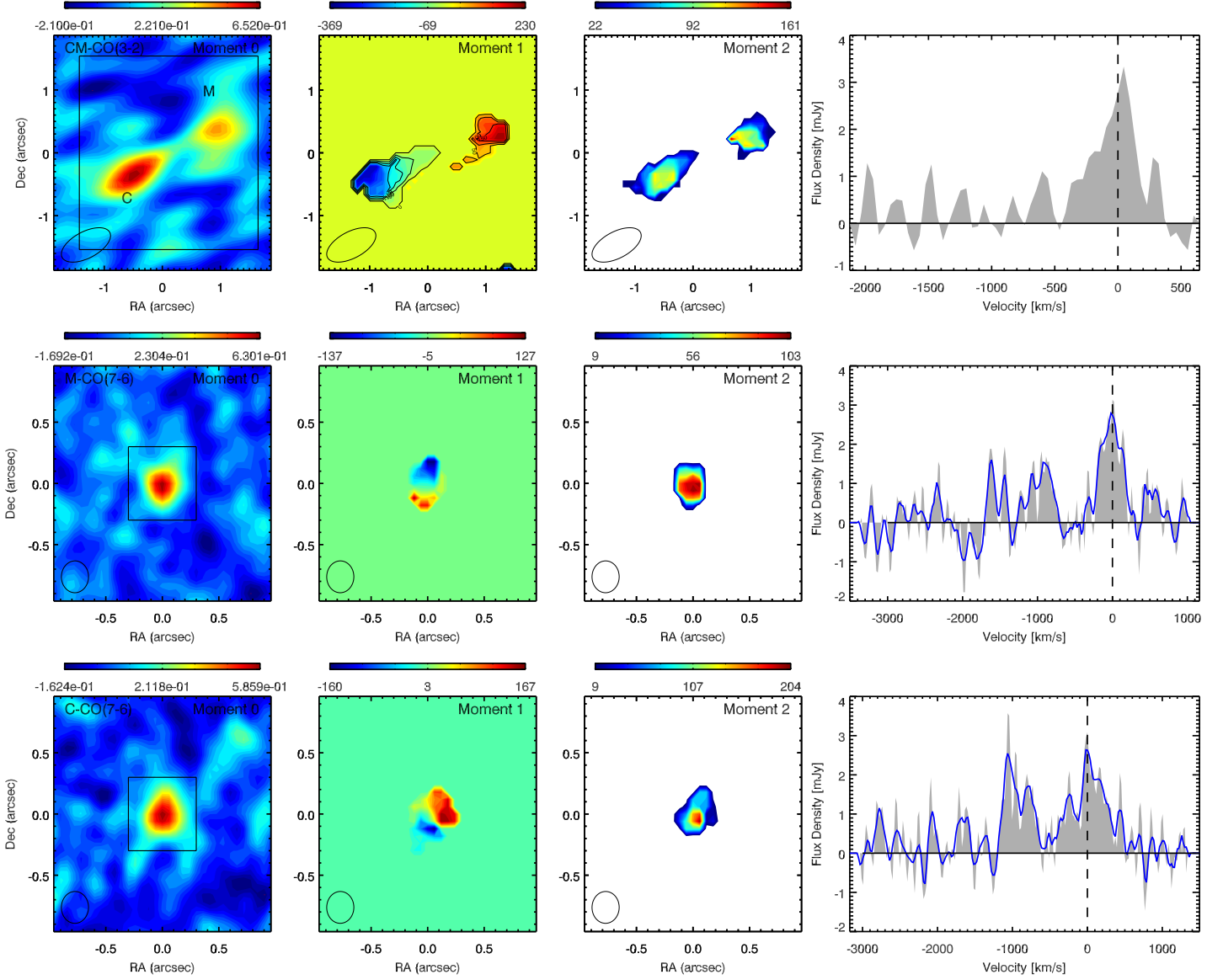


Fig. 9. Similar to Fig. 7 but for components M and C. The top row shows the results for the CO J:3–2 line in both M and C together. The middle and bottom rows show the results for the CO J:7–6 line separately for components M and C, respectively. In the right-most panels of the middle and bottom rows (the galaxy-integrated profiles of the CO J:7–6 lines in M and C, respectively) the CO J:7–6 line covers a velocity range of approximately ± 300 km s $^{-1}$ and 500 km s $^{-1}$, respectively. For both components the [C I] $^3P_2 \rightarrow ^3P_1$ line is also clearly visible at lower (~ 1000 km s $^{-1}$ to the blue) velocities. We do not show the equivalent moment maps for the [C I] $^3P_2 \rightarrow ^3P_1$ line in M and C as they are significantly noisier.

solid body rotation at small radii and a flat rotation curve at larger radii:

$$V_{\text{radial}} = \begin{cases} V_{\text{slope}} \cdot r \cdot \cos(\phi) \cdot \sin(i) & \text{if } r \leq r_{\text{flat}} \\ V_{\text{slope}} \cdot r_{\text{flat}} \cdot \cos(\phi) \cdot \sin(i) & \text{if } r > r_{\text{flat}} \end{cases} \quad (3)$$

where V_{radial} is the observed radial velocity in km s $^{-1}$, V_{slope} is the slope of the solid body rotation in the inner region (km s $^{-1}$ kpc $^{-1}$), r (kpc) and ϕ (degrees) are the polar coordinates in the disk of the galaxy, and r_{flat} is the radius at which the solid body rotation changes to a flat rotation curve. The model is initially constrained using the *Kinometry*-derived parameters (Tables 4 and 5). The kinematic centre derived by *Kinometry* was used for each galaxy, and we varied the values of V_{slope} and r_{flat} so as to get the best agreement (via visual inspection) between the toy

model, the velocities seen along the major axis of each component, and the rotation curve produced by *Kinometry*. We use this toy model for all further analysis (e.g. residual velocity maps) as it relatively well follows the *Kinometry*-derived model but smooths out the small-scale variations of the latter (which are most likely caused by signal-to-noise and resolution limitations, rather than being true physical features).

The results of the rotation-only modelling of components W and T are shown in Figs 10 and 11, respectively. For both components W and T, the *Kinometry* analysis and thus the rotation-only models are very similar for both CO J:7–6 and [C I] 2–1. The models for CO J:3–2 also give similar PAs and inclinations, but the best-fit rotation curve is relatively smooth, as expected given the lower spatial resolution of the data. In Figs 10 and 11 we also present (in the third column) the residuals between the observed velocity field and the toy model velocity field, i.e. $V_{\text{galaxy}} - V_{\text{model}}$,

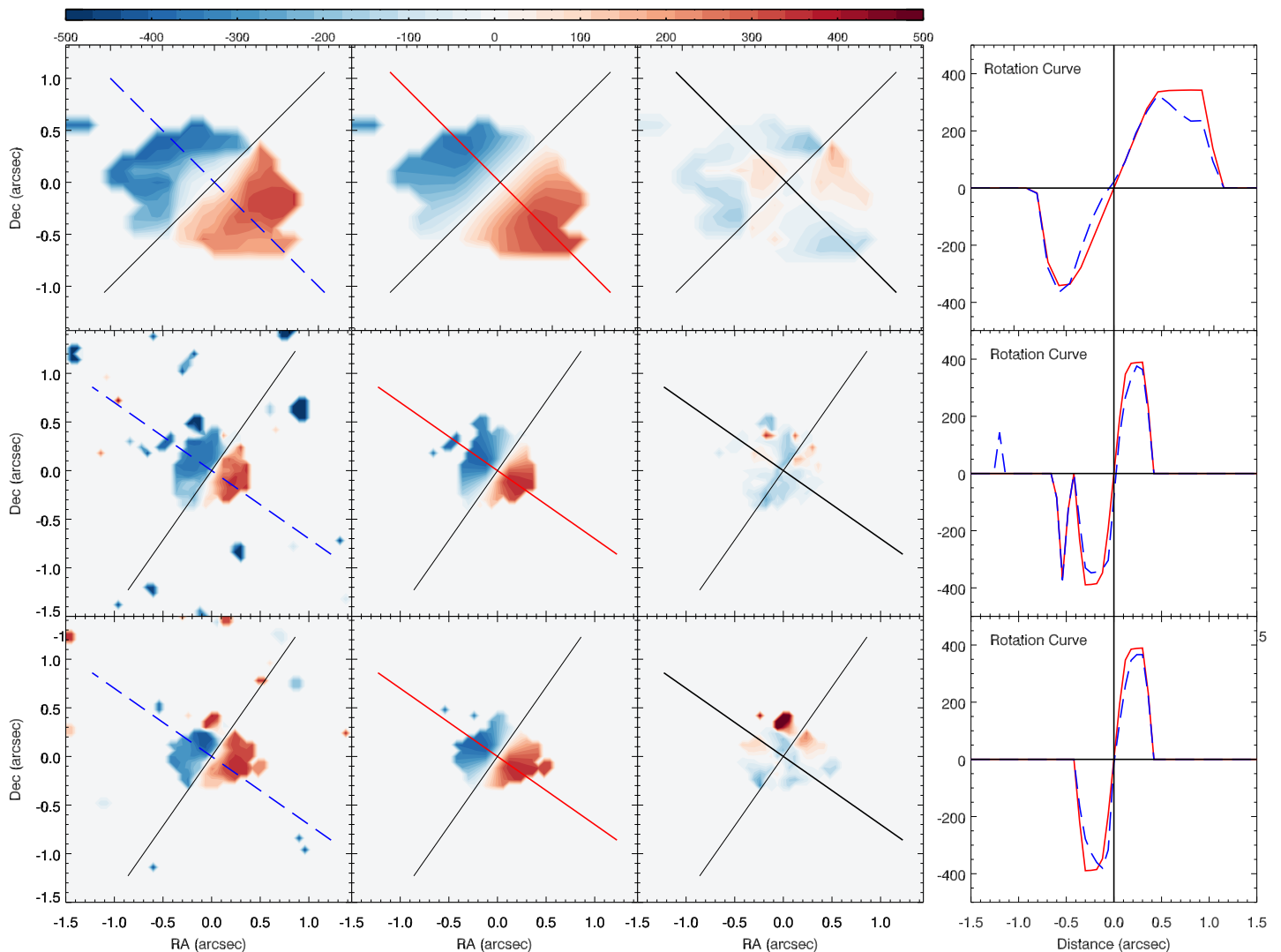


Fig. 10. Results from the rotation-only modelling of the kinematics of component W. From left to right: the observed velocity (moment 1) maps, our rotation-only model (based on parameters derived from *Kinemetry*; see Section 3.2), the velocity field residuals (observed velocity field minus the rotation-only model), and our derived rotation curves for, top to bottom: CO J:3–2, CO J:7–6 and [C I] 2–1. Each observed velocity field was input to the *Kinemetry* package to determine the kinematic PA and inclination (see text): these independently derived values are similar for all lines except CO J:3–2. The pure rotation models were then constructed (by eye) using these values of PA and inclination together with a simple model of solid body rotation which changes to a flat rotation beyond a certain radius. In the left three columns, the colours follow the common colour bar (in km/s) at the top, and areas with low signal to noise in the moment 0 map are masked. The lines denote the major and minor axes, respectively. The rotation curve panels show the observed radial (i.e. projected) velocity along the major axis in km s^{-1} on the y-axis (blue dashed line) and the model rotation curve (red solid line).

in order to highlight deviations from pure rotation. The residuals are typically $\lesssim 50 \text{ km s}^{-1}$, and there are no immediately obvious patterns of ordered non-circular motions. For example, outflows in the disk could show opposite colours along each half minor axis, a signature not seen in the residual velocity fields.

3.5. Non-circular Disk Kinematics: testing for outflows and P Cygni profiles

Position-velocity (PV) diagrams of all four detected lines are shown in Figs 12 and 13) for components W and T, respectively. The PV diagrams were extracted along the kinematic major and minor axes discussed in the previous section: kinematic major axes PAs of 55° and 135° for W and T, respectively; see Figs 10 and 11), using a pseudo-slit of width $0.06''$ for CO J:7–6, and

[C I] 2–1, and $0.11''$ for CO J:3–2; they are thus limited in spatial resolution by the intrinsic spatial resolution of the images. On each PV diagram we have overlaid the predictions of our toy rotation model (black dashed line) described in Section 3.4. Along the major axis, in both W and T, the toy rotation model follows well the velocity structure of the CO and [C I] 2–1 gas: in fact, especially in CO J:3–2, one can discern the point at which the presumed rotation changes from solid body to flat. The gas velocities do show interesting wiggles away from the prediction of the rotation model – see e.g. the radii close to the nucleus and to the SW in the CO J:3–2 major axis PV diagram – but a higher spatial resolution and signal-to-noise is required to model these deviations. The kinematic signatures of W and T in their PV diagrams along the posited kinematic major axis, specifically the velocity gradient seen close to the nucleus, is a strong argument

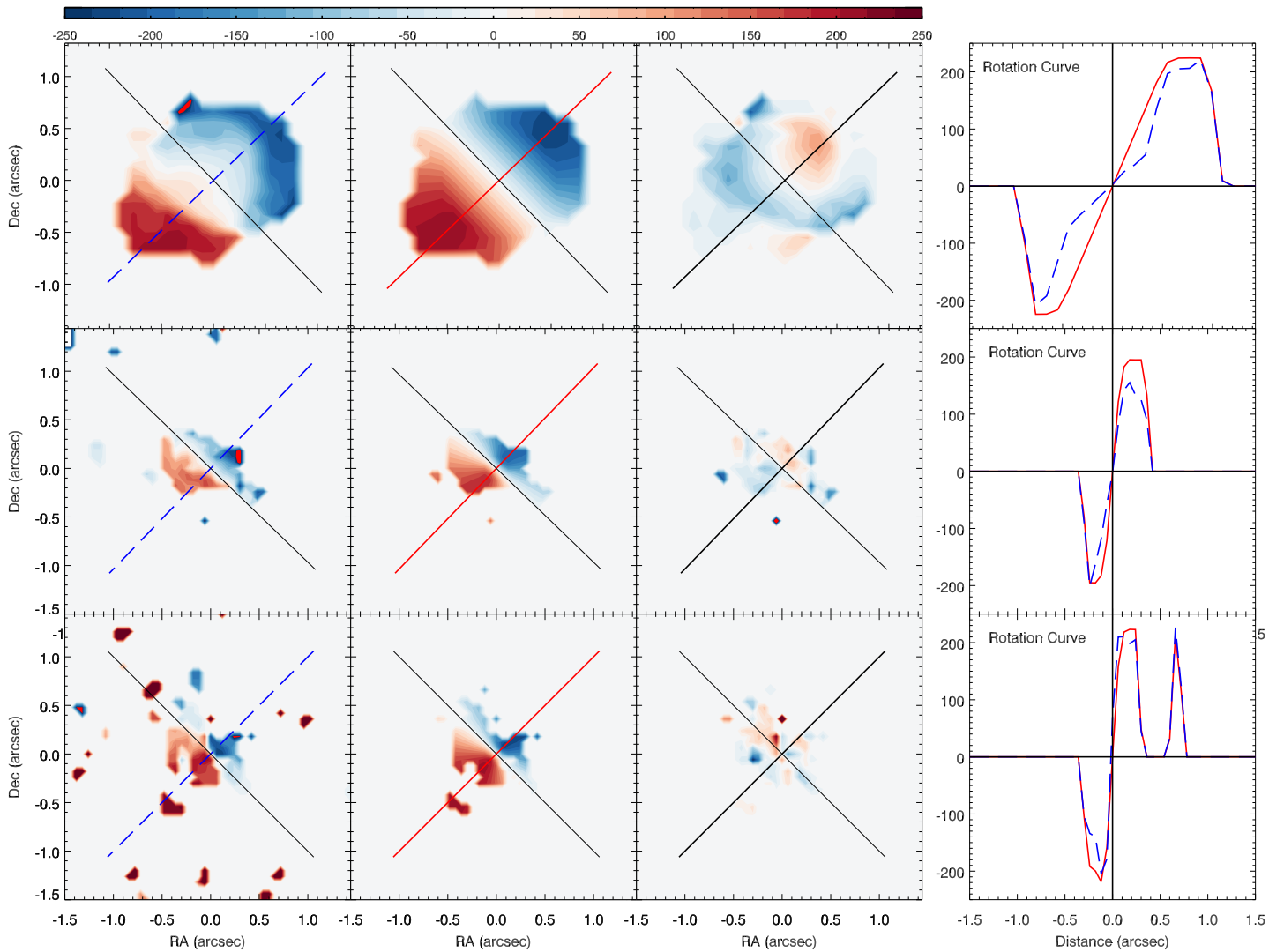


Fig. 11. As in Fig. 10 but for component T of HATLAS J084933.4+021443

that the kinematics is rotation-dominated. Outflows within the disk would produce a more abrupt change in velocity from one side of the disk to the other. Along the kinematic minor axes of W and T, the data are more difficult to interpret: we expect to see zero velocities at all offsets but smearing from the relatively large synthesised beam means that multiple velocity components are seen in all spatial offsets along the minor axis. This is unfortunate since any outflow within the plane of the disk would be most apparent along the minor axis. In W, the minor axis PV diagram of the CO J:3–2 line shows a $\sim 100 \text{ km s}^{-1}$ feature to the SE. In fact this distortion in the zero-velocity line is also clearly seen in the equivalent velocity field (e.g. top row of Fig. 10). The equivalent, but fainter, blueshifted component is seen to the NW. This could trace a molecular outflow in the disk if the SE is the far side of the disk. However, many alternative explanations are possible, including bar driven distortions in the gas kinematics and thus we cannot at this point present evidence for outflows or inflows.

The PV diagrams presented here are also useful to highlight the different kinematics seen in the water vapour line. In W, the water vapour line appears to follow the expectations of the rotation model, but in the case of T the water line does not appear to follow rotation along the major axis and its velocities along the

minor axis are marginally larger than that seen in the other lines. A potential explanation is that this line comes from outflowing gas: given the PV diagrams presented here, and the velocity and dispersion maps presented in the previous sections, the outflow velocities are likely to be predominantly spherical in component T.

P-Cygni (or simple absorption-line) profiles are potentially detected at similar velocity offsets (from systemic) in all of CO J:7–6, [C I] 2–1 and H₂O. To quantify if any of these can be fit with a single velocity absorption line component, we modelled the combined galaxy-wide CO J:7–6 and [C I] 2–1 spectrum of T with a sum of emission line and absorption line components. The best-fit model is created as follows: we use the sum of five Gaussian components to fit the CO J:7–6 line profile: one emission line centred at systemic velocity and 4 absorption lines centred at the most promising (by eye) potential absorption lines. The free parameters are thus the amplitude and width (σ) of each of the five Gaussians. Since the CO J:7–6 and [C I] 2–1 lines overlap we are forced to fit them together. We thus add to the model five more Gaussians to recreate the [C I] 2–1 line, whose parameters are completely tied to the first five Gaussians: the offset between each pair of emission and absorption Gaussians is fixed to 1051 km/s, which corresponds to the velocity offset

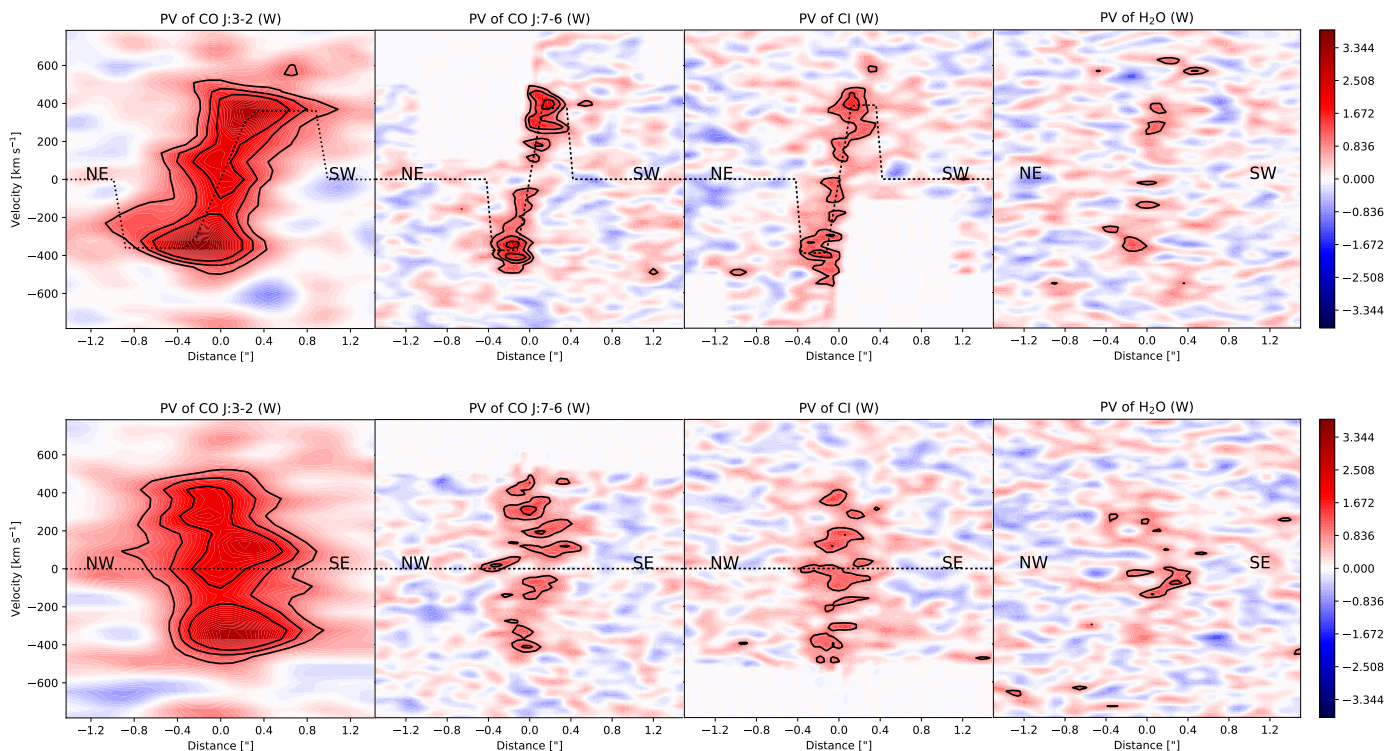


Fig. 12. Position-velocity (PV) diagrams for (left to right) the CO J:3–2, CO J:7–6 and [C I] 2–1 emission lines in component W are shown in colour following the common colour bar to the far right of each row (flux in units of $\text{mJy km s}^{-1} \text{beam}^{-1}$) and in black contours ($1, 1.5$ and $2 \text{ mJy km s}^{-1} \text{beam}^{-1}$). At our adopted distance for HATLAS J084933, $1''$ corresponds to 8.25 kpc . The top (bottom) row shows the PV diagram along the major (minor) axis of component W. The dashed black lines show the predictions of our adopted rotation model (see Sect 3.3).

between the CO J:7–6 and [C I] 2–1 lines, the amplitude ratio between each Gaussian pair is a single new free parameter, and the widths of the new five Gaussians are fixed to the widths of the original five Gaussians. Thus the summed model of the [C I] 2–1 profile is merely a shifted (at a fixed velocity) and scaled (a single amplitude scaling for all five new Gaussians) copy of the summed model used for the CO J:7–6 line, and the total number of free parameters is 11 (the widths and amplitudes of the first five Gaussians, and the global amplitude scaling factor between the five Gaussians used to recreate CO J:7–6 and the five Gaussians used to recreate [C I] 2–1). We then use a minimised Chi-square (χ^2) method to determine the model which best fits the observed line profile.

The best fit model profile obtained is compared to the observed spectrum of T in the right panel of Fig. 14. The best-fit parameters for the CO line are as follows: (a) emission line with a FWHM of 534 km/s (fitted) and amplitude 9.11 mJy (fitted); (b) absorption lines centred at velocities of $-390, -200, +50$ and $+450 \text{ km/s}$ (fixed) with amplitudes of $2.59, 2.01, 4.27,$ and 4.45 mJy (fitted) and FWHMs of $106, 47, 52$ and 118 km/s (fitted), respectively. Finally a value of 0.75 (fitted) is obtained as the scaling factor in converting the above (CO) Gaussians to the Gaussians used to form the [C I] 2–1 line profile; this scaling also matches that obtained in component W.

The only consistent absorption line is that at 450 km/s , whose FWHM is 118 km s^{-1} . This is present in both emission line profiles, even when these are smoothed to spectral resolutions of $\approx 100 \text{ km/s}$ (see figure 8). The spectrum of the nuclear aperture (left panel of Fig. 14) also shows these absorption components but they are not as strong as in the global spectrum. If true, this would imply a P-Cygni-like spectrum but tracing absorption in

an inflow, which is highly unlikely. In any case, given the many other potential absorption features seen in the profiles we cannot make any definitive statement on the reality of this absorption line.

3.6. Resolved Line Ratios: gas excitation and [C I] 2–1 as a tracer of molecular gas

Resolved line luminosities for CO J:3–2, CO J:7–6, [C I] 2–1, and H_2O were calculated as in Section 3.1 but instead of galaxy- and velocity-integrated line fluxes, we use velocity-integrated fluxes extracted in apertures equivalent to the synthesised beam size (FWHM), and spaced by half a synthesised beam. As before, for the two line emission two maps involved, the higher resolution map was convolved with a Gaussian in order to degrade the resolution to that of the lower resolution map. Note that latter three lines have very similar resolutions; however, when comparing CO J:3–2 and CO J:7–6, the synthesised beam sizes are highly different. Thus, extra caution is required when comparing CO J:3–2 and CO J:7–6, and thus interpreting the CO ladder excitation. Figure 15 shows the relationship between the kpc-scale resolved CO J:7–6 luminosity and the luminosities of the CO J:3–2, [C I] 2–1, and H_2O emission lines. The best fits to the data from individual apertures (dashed lines) and the prediction of the galaxy-integrated ratios (solid lines) are shown for easy comparison. The galaxy-integrated [C I] 2–1 to CO ratios are driven by a few dominant apertures: the resolved ratios of [C I] 2–1 to CO J:3–2 show a dependence which is significantly sub-linear. The resolved ratios of [C I] 2–1 to CO J:7–6 are also sub-linear, though not as much as in the case of using CO J:3–2: the resolved [C I] 2–1 luminosity is typically ~ 0.1 dex (W) or

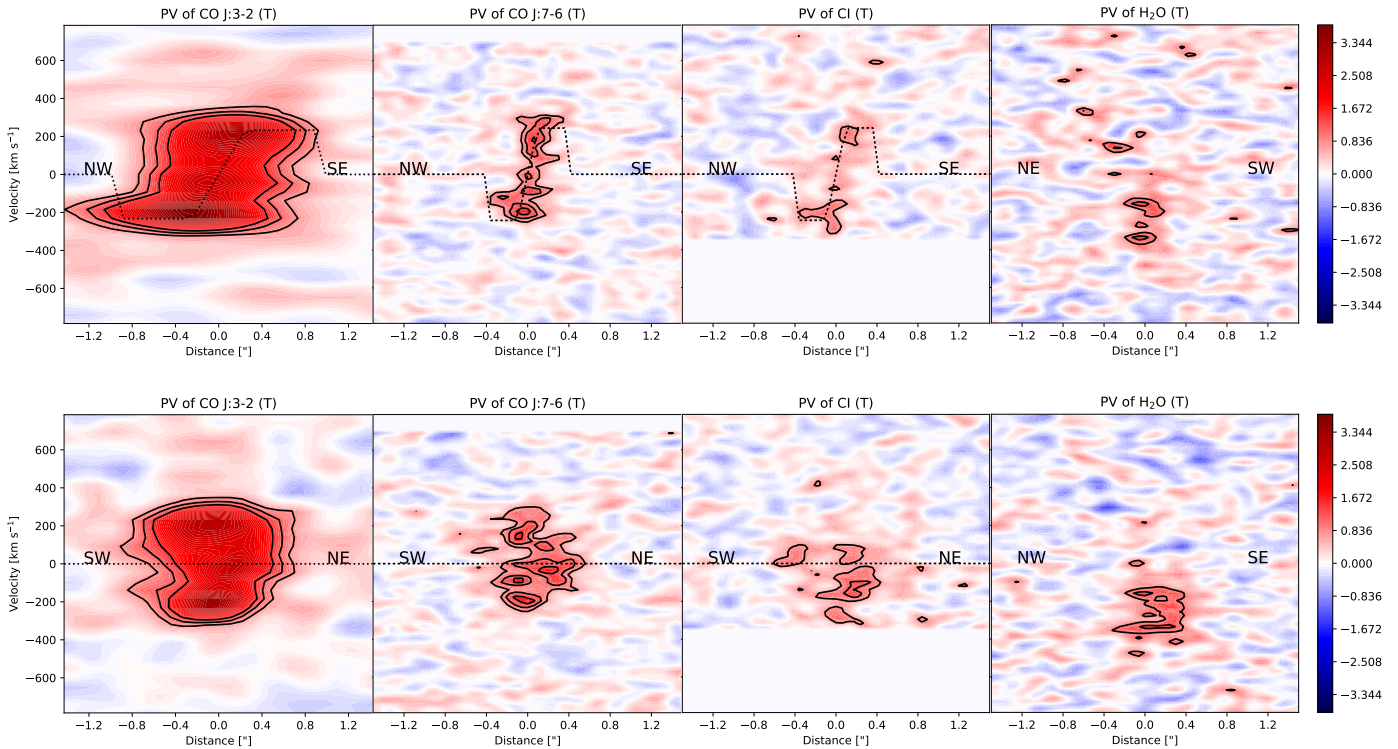


Fig. 13. As in Fig. 12, but for component T.

0.2 dex (T) lower than the value which would be estimated by the galaxy-integrated line ratio. This is loosely consistent with our finding that the [C I] 2–1 line emission is slightly more extended (at relatively low fluxes) than CO J:7–6. Further, recall that the [C I] 1–0 line is typically used to trace molecular (or CO) gas. Using the [C I] 2–1 line requires assuming an excitation temperature (where a higher temperature implies more [C I] 2–1 emission per unit C I mass). Thus converting a CO J:7–6 to [C I] 2–1 ratio to a CO to C I gas mass ratio requires information on temperature and density, and the sub-linear relationship we see may thus be mainly an effect of physical conditions in the gas.

The resolved CO J:7–6 to CO J:3–2 ladder also shows deviations from the galaxy-integrated value, but the relatively large error bars, and the highly mismatched synthesised beams of the two maps makes interpretation of this figure difficult. The relationship between CO J:7–6 and water vapour shows a lot of scatter as expected, though surprisingly the best fit to the scattered points gives an almost linear relationship between the two luminosities.

Thus overall, [C I] 2–1 is a relatively good, almost linear, tracer of dense/warm (as traced by CO J:7–6) molecular gas in both W and T, though as discussed here and in previous sections, there are mismatches in the morphology of the C I and CO J:7–6 in both W and T. Due to assumptions of the CO ladder and excitation temperature of C I, we are unable to evaluate the relationship between C I and CO mass.

3.7. A resolved (2 kpc-scale) warm/dense gas Schmidt-Kennicutt Relationship

Given that we have both resolved estimators of molecular gas mass (CO J:3–2, CO J:7–6 and [C I] 2–1) and resolved estimators of the IR luminosity, thus SFR (the rest-frame 1160 GHz

continuum luminosity), it is highly relevant to test the relationship between the two both as global quantities and as surface densities.

We first outline the approximations and estimations required to be made. First, we use the values derived by I13 for the galaxy-integrated molecular gas mass (derived from CO J:1–0 imaging) and total (rest-frame 8–1000 μm) IR luminosity (from detailed SED fitting) for both W and T. Our resolved CO J:7–6 (or [C I] 2–1) and rest-frame 1160 GHz continuum images are used to distribute these global values over individual resolved apertures, i.e. a relative, and not absolute, distribution. In other words, we assume that the rest-frame 1160 GHz (260 μm ; close to the IR peak; see I13) luminosity closely traces – in a relative sense – the distribution of the IR luminosity, and that the CO J:7–6 map closely traces – in a relative sense – the distribution of molecular gas. Once more, as for the continuum maps in Fig. 4, we use apertures with size equal to the ALMA synthesised beam in the CO J:7–6 and [C I] 2–1 maps, spaced by half a beam width. The resulting conversion factors between total continuum luminosity at 1160GHz (in units of $L_{\odot} \text{Hz}^{-1}$) and total L_{IR} (in units of L_{\odot}) for the galaxies W and T are

$$L_{\text{IR}} = \frac{2.414 \times 10^{-14}}{[\text{Hz}^{-1}]} L_{1160\text{GHz}} \quad (4)$$

and

$$L_{\text{IR}} = \frac{2.256 \times 10^{-14}}{[\text{Hz}^{-1}]} L_{1160\text{GHz}}, \quad (5)$$

respectively. The conversions are different at the 10% level as each galaxy has a different global IR (from I13) to $L_{1160\text{GHz}}$ (this work) ratio, reflecting the different shapes of their SEDs.

We then use this value of L_{IR} to estimate the resolved SFR using the relationship of Kennicutt (1998), which assumes a

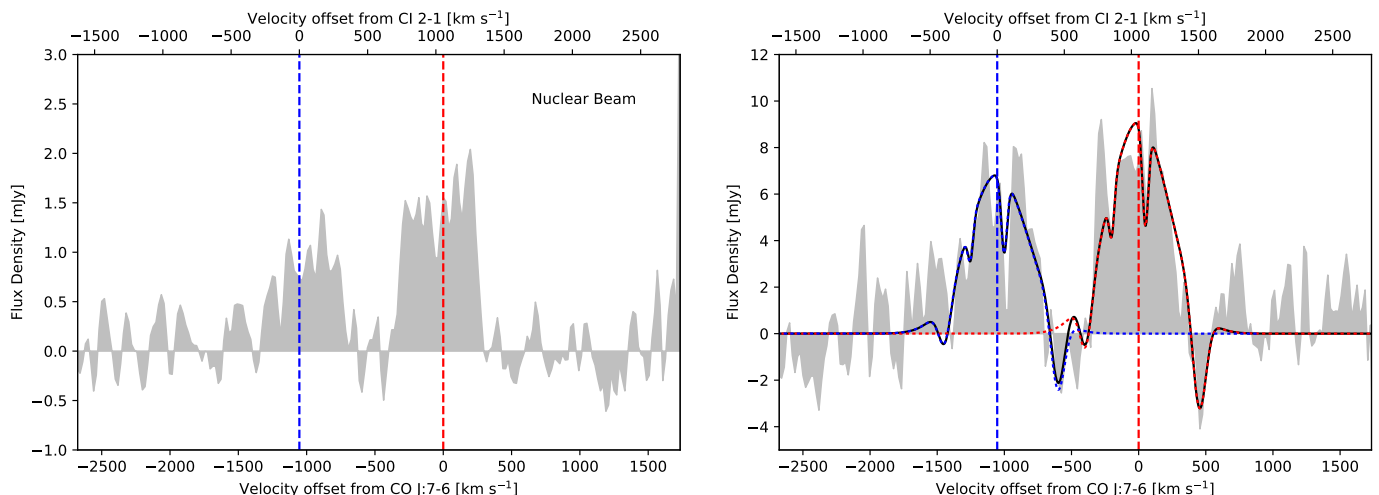


Fig. 14. Potential absorption components in CO and [C I]: each panel shows a spectrum of component T covering the CO J:7–6 (left) and [C I] 2–1 (right) emission lines at a resolution of 19.7 km s^{-1} per channel (grey filled region). The dashed blue line marks the 0-velocity of the [C I] 2–1 frequency at $z = 2.41$ (scale on the top y-axis), and the dashed red line marks the zero-velocity for the CO J:7–6 line at the same redshift (scale on the bottom y-axis). The left panel shows a nuclear spectrum of T while the right panel shows a galaxy-integrated spectrum of T. In the right panel, the solid red line shows the best fit spectrum to the CO J:7–6 line profile: the starting model was the sum of a Gaussian emission component at the rest frequency of the line (0 km s^{-1}) plus four Gaussian absorption components at velocities fixed (by eye) to -385 , -225 , $+80$ and $+455 \text{ km s}^{-1}$. The amplitudes and widths of each of the five components were then varied to achieve the best fit using r.m.s. minimisation. The equivalent solid blue line for [C I] 2–1 is obtained from the best fit CO J:7–6 spectrum but using a displacement of -1051 km s^{-1} (based only on the frequency difference between the lines) and an amplitude scaling of 0.7 for each emission and absorption component. The black solid line represents the sum of the best fit to the CO J:7–6 and [C I] 2–1 profiles (sum of the red and blue spectra; this summed spectra is often not visible as it often lies under the blue and red solid lines). The only relatively consistent and significant absorption component is that at $+455 \text{ km s}^{-1}$.

Salpeter IMF:

$$\text{SFR} [\text{M}_{\odot} \text{yr}^{-1}] = \frac{L_{\text{IR}}}{5.8 \times 10^9 [L_{\odot}]} \quad (6)$$

The SFR surface density, when required, is calculated using the linear size of the synthesised beam.

For molecular gas masses, we have three alternatives to derive the gas mass in each aperture, all of which use the galaxy-integrated CO mass derived by I13 together with an estimated resolved map of the CO J:1–0 emission:

1. using the resolved CO J:7–6 flux map and the galaxy-integrated CO J:7–6 to CO J:1–0 ratio to derive a CO J:1–0 luminosity map (i.e. assuming that the galaxy-integrated CO ladder is valid for each resolved aperture of a given galaxy);
2. using the resolved CO J:7–6 luminosity map, together with the linear fit to the relationship between the resolved (see Fig. 15) CO J:7–6 and CO J:3–2 line luminosities, to derive an estimated resolved CO J:3–2 luminosity map. This is then converted to a CO J:1–0 luminosity map assuming thermally excited gas, as evidenced in Fig. 3. This method should be more reliable than (a) above since we know that the CO J:7–6 to CO J:3–2 ratio varies over the galaxy (Fig. 15) while the CO J:3–2 to CO J:1–0 ratio is more likely to be constant in SMGs;
3. using the resolved [C I] 2–1 luminosity map, together with the galaxy-integrated [C I] 2–1 to CO J:1–0 luminosity ratio to create an estimated map of the CO J:1–0 luminosity.

All three alternatives give consistent results, so here we show the results of using method (a) above. We use the galaxy-integrated CO ‘ladder’ of the individual components (see Fig. 3) to obtain the following for component W: $S_{\text{CO J:7-6}}/S_{\text{CO J:1-0}} \sim 5.52 \pm 1.64$, thus $L'_{\text{CO}} = (8.87 \pm 2.57) \times L'_{\text{CO J:7-6}}$ and $M_{\text{mol}} =$

$(7.10 \pm 2.06) \times L'_{\text{CO J:7-6}}$. For the other components, the equivalent conversions are as follows. Component T: $M_{\text{mol}} = (8.06 \pm 1.77) \times L'_{\text{CO J:7-6}}$, Component M: $M_{\text{mol}} = 4.85 \pm 0.87 \times L'_{\text{CO J:7-6}}$, and Component C: $M_{\text{mol}} = 6.06 \pm 0.13 \times L'_{\text{CO J:7-6}}$.

Fig. 16 shows the dependence of the resolved IR luminosities on the CO and [C I] 2–1 emission line luminosities. When using CO J:3–2 on the x -axis (as a proxy for gas mass), both W and T follow relatively well the (galaxy-integrated) relationships (slope ~ 1.2) found by Daddi et al. (2010) and Genzel et al. (2010) (cf. Ivison et al. 2011) for nearby and high-redshift star-forming galaxies: in this scenario, most apertures in W are consistent with being on the ‘luminous starburst’ sequence while most apertures in T lie between the supposed sequences for luminous starbursts and ‘normal star-forming’ galaxies. The dependence of the IR luminosity on warm and dense gas mass (using CO J:7–6 or [C I] 2–1 as a proxy) is significantly steeper than the case of CO J:3–2: the slope of the relationship is now between ~ 1.5 and ~ 2.5 , and W and T are relatively indistinguishable in these plots. This is unusually steep given that previous works have found that the dependence of IR luminosity on dense gas mass (via HCN J:1–0) is linear when galaxy-integrated quantities are taken into account (Gao & Solomon 2004; Shimajiri et al. 2017; Oteo et al. 2017), though this relationship is not necessarily universal: Liu et al. (2016) find that the relationship is sub-linear in resolved clumps in the Galaxy. Since we are tracing both warm and dense gas with CO J:7–6, rather than only dense gas as in the case of HCN J:1–0, the steep dependence is potentially an effect of varying temperature and density across the apertures, i.e. in higher temperature dense regions the dependence of CO J:7–6 luminosity on SFR is steeper (the sub-mm emission would not be expected to change by a large factor, given the relatively uniform sub-mm spectral slopes seen over the galaxy). The slopes seen here are not the result of systematic differences in the SNR and beam shape in the individual

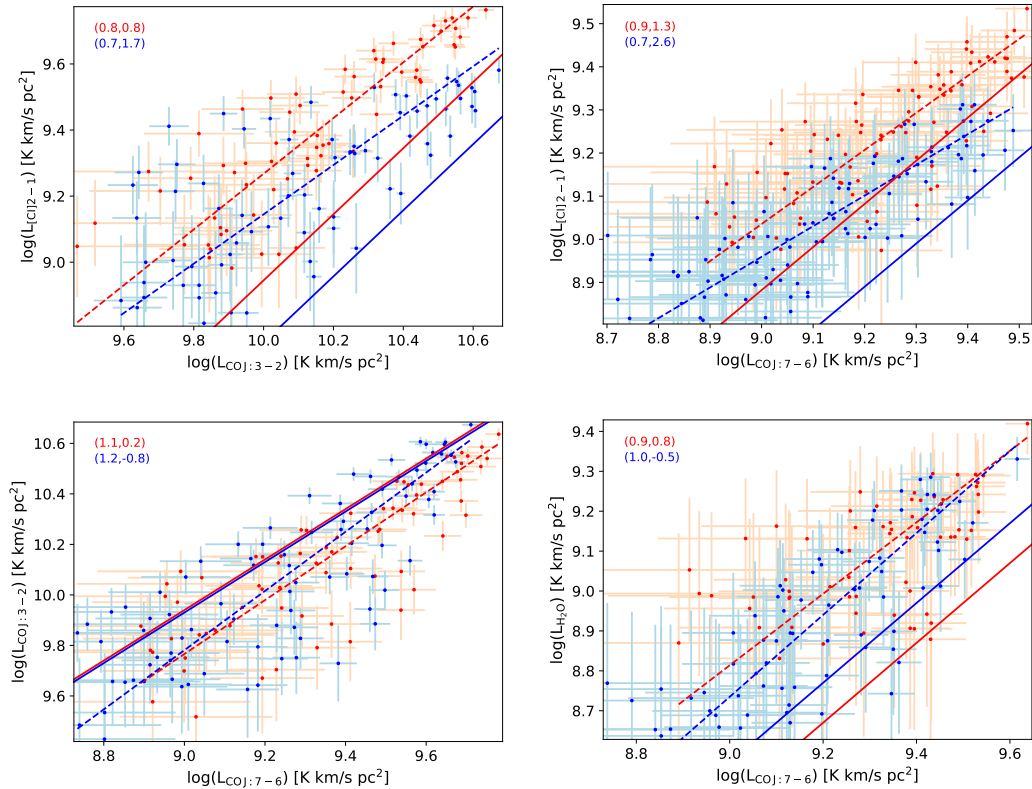


Fig. 15. As in Fig. 4, but here we compare the emission line luminosities (L'_{line} from eqn. 3) of CO J:3–2, CO J:7–6, [C I] 2–1, and H₂O. In each panel the solid lines in the corresponding colour show the prediction if the galaxy integrated line flux ratio was valid over all individual apertures.

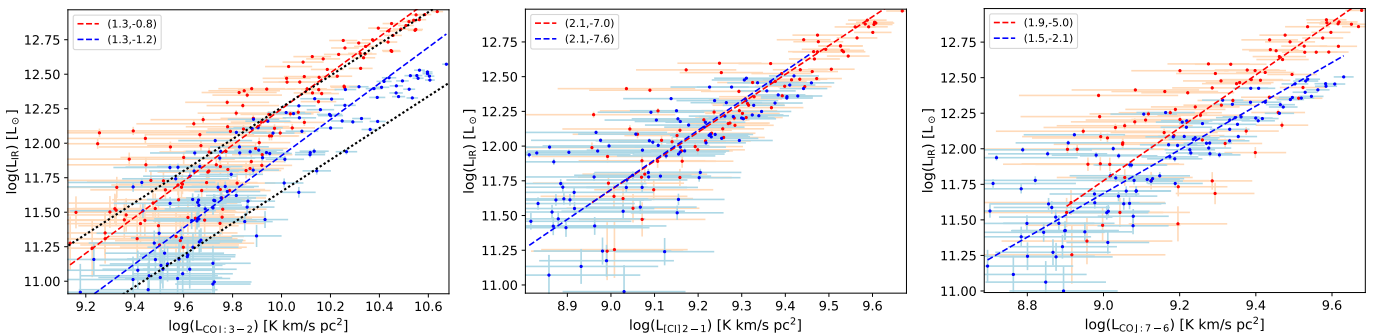


Fig. 16. As in Figs 4 and 15, but here we show the correlation between the resolved IR luminosity (estimated from the resolved rest-frame 1160 GHz continuum map; see text) and the luminosities (L'_{line}) of the CO J:7–6, [C I], and CO J:3–2 lines. In the left panel the black dashed lines show the galaxy-integrated relationships derived by Daddi et al. (2010) and Genzel et al. (2010) for normal star-forming (lower line) and ‘starbursting’ (upper line) galaxies; here we assumed thermally excited gas, i.e. $L'_{\text{lineCOJ:3-2}}/L'_{\text{lineCOJ:1-0}} = 1$.

maps. Constructing the same figures but using regions between the galaxies (i.e. ‘empty sky’ in the ALMA maps) shows that the data cluster around [0,0] without any noticeable systematics.

Converting the relationships between IR luminosity and gas (CO or [C I] 2–1) luminosity into a resolved Schmidt-Kennicutt relationship is trivial in our case since all data have the same aperture size: the conversion to gas mass (instead of luminosity) and surface density (division by linear aperture size) only involves a change in the axis units. Nevertheless, for easier understanding, we show, in a new figure (Fig. 17) the resolved Schmidt-Kennicutt relationship ($\Sigma_{\text{SFR}} \propto \Sigma_{\text{H}_2}^N$) for components W and T in the case of using CO J:7–6 to predict the gas surface density, i.e. using a warm/dense gas tracer, instead of a cold

molecular gas tracer like CO J:1–0. Not surprisingly the resolved warm/dense gas SK relationship in W and T are ~ 1 dex higher than the cold SK relationship seen in nearby galaxies (solid back line in the figure). Our data cover similar parameter space as those of the few previous determinations of the resolved SK relationship in high-redshift galaxies (Thomson et al. 2015; Freundlich et al. 2013). Component W shows slightly higher star-formation efficiencies than T, with most apertures within 0.5 dex of a gas exhaustion time of ~ 1 Gyr. Not surprisingly, the highest efficiencies are in the nuclei.

SK-type power-law fits to the data for W and T in Fig. 17 result in significantly different slopes depending on the specific fitting routine used. This is due both to the large spread of data

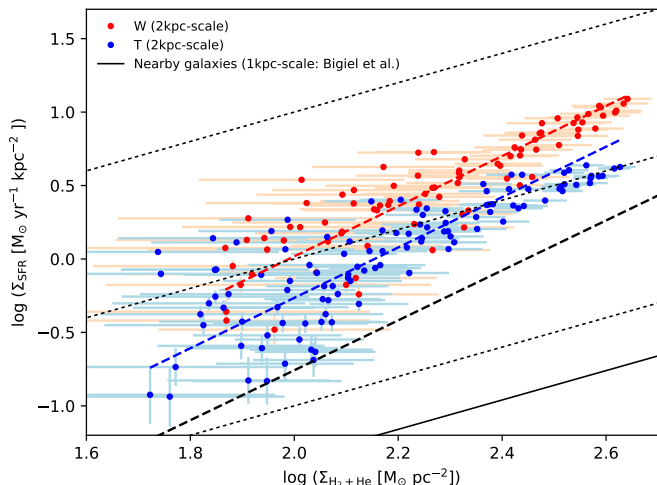


Fig. 17. The resolved Schmidt-Kennicutt relationship equivalent for warm/dense molecular gas, i.e. the relationship between the surface densities of star formation and warm/dense molecular gas (as traced by CO J:7–6), for components W (red points) and T (blue points). Each data point was calculated over an aperture equivalent to the (FWHM) synthesised beam (roughly 2 kpc), with a spacing of half a synthesised beam between points, i.e. roughly a quarter of the points are independent measurements. The star-formation rate is estimated from the resolved rest-frame 1160 GHz continuum map and the molecular gas mass from the resolved CO J:7–6 emission line map and standard conversions of this to CO J:1–0 and thus gas mass (see text). The solid black line at the bottom-right is the kpc-scale resolved (cold gas, i.e. as derived from CO J:1–0) SK relationship in nearby ‘normal’ galaxies Bigiel et al. (2011). The dotted lines delineate gas exhaustion times of (top to bottom) 0.1, 1, and 10 Gyr and the blue and red dashed lines show illustrative SK relationships with slopes 1.72 ± 0.24 and 1.71 ± 0.26 , respectively (see text). For component T we used the observed (image plane) linear sizes corresponding to the synthesised beam; if the image plane is spatially stretched due to lensing then the individual points will move towards the top right, parallel to the dashed lines (constant gas exhaustion times) in the figure, further differentiating them from the data points for component W.

points in the bottom left quadrant of the figure, and the fork shape seen in the red points at higher gas surface densities. Fits to the W (red) data points typically give slopes of 1.71 ± 0.26 , while fits to the T (blue) data points give slopes of 1.72 ± 0.24 . In all cases the slopes are greater than 1.5. The intercepts ($\log A$ in the SK equation) are relatively invariant with values of ~ -3.4 and ~ -3.7 for W and T, respectively. Thus, in both W and T, the resolved warm/dense gas SK relationship follows a power law with slope ~ 1.7 (red and blue dashed line), significantly steeper than seen previously in cold gas SK relationships in low- or high-redshift galaxies.

How reliable is this finding of a steep slope in the warm/dense gas SK relationship? The variations in the slopes discussed above result from the measurement and linear fitting errors only, without taking systematic uncertainties into account. It is thus relevant to examine the systematic uncertainties in deriving the two quantities used in the figure: SFR and gas mass. The total IR luminosity is the most reliable estimator of SFR (e.g., Kennicutt & Evans 2012) – more reliable than, e.g., an SFR estimation from the $H\alpha$ emission line luminosity as used by Freundlich et al. (2013), and we emphasise that the galaxy-integrated IR luminosities of W and T were derived from the

comprehensive SED analysis of I13. Ideally, the SFR is derived from a combination of IR and UV luminosities ($2.2 L_{\text{UV}} + L_{\text{IR}}$), where the UV luminosity can be obtained by, e.g., $1.5 \nu L_{\nu}$ at 2800\AA (Bell et al. 2005). Using the galaxy-integrated rest-frame-UV (2600\AA) fluxes listed in I13 for W and T (see their Table 1 and Fig. 2), L_{UV} comes out to ~ 1 to 2% of L_{IR} for both W and T. The UV luminosity is thus unlikely to cause significant differences in any aperture of W and T and is thus safe to ignore. An additional systematic in the derivation of our resolved SFRs is the use of our rest-frame $250 \mu\text{m}$ (which is longward of the IR peak) ALMA map to distribute the total SFR into individual apertures. For dust at a known single temperature, which appears to be the case in component W (Fig. 4 and related discussion), the $250 \mu\text{m}$ flux is a good tracer of the IR luminosity in an absolute and relative sense (e.g., Orellana et al. 2017). For multiple dust temperatures, as is likely the case in component T (Fig. 4 and related discussion), systematics would be expected. If the hotter dust component(s) is due to star formation, then we are underestimating the SFR in the nuclear regions (so that the true SK relationship in T would have an ever steeper slope); if the hotter dust component(s) is due to an AGN (for which deep *XMM-Newton* imaging provides no evidence – Ivison et al., in preparation) then we are over-estimating the SFR in the nuclear regions, so that the intrinsic SK relationship in T is shallower than ~ 2 . Resolved maps of the IR continuum shortward of the IR peak would be required to resolve this. Thus, in comparison to equivalent relevant studies at high redshift, our resolved SFR estimations are among the most reliable.

For resolved gas masses, the systematics are likely larger, though here too we have the advantage of having multiple tracers of molecular gas (CO and [C I] 2–1). The galaxy-integrated gas mass has been derived in I13 from CO J:1–0 imaging and an α_{CO} of 0.8. This total mass has been distributed into resolved apertures using our resolved CO J:7–6 or [C I] 2–1 maps. A varying α_{CO} within an individual galaxy, or a highly varying CO ladder over the individual apertures, would be required to change the slope of the resolved warm/dense gas SK relationship that we find.

4. Summary

We present new resolved imaging of the continuum and emission lines in the four known components of the binary HyLIRG, HATLAS J084933.4+021443 at $z = 2.41$. The new imaging allows us to further extend the comprehensive characterisation of this system presented in I13.

Our main results are:

1. All four component galaxies of HATLAS J084933.4+021443 (W, T, M and C) are spatially (~ 0.3 or 2.5 pc) resolved in CO J:7–6, [C I] 2–1, and the sub-mm continuum. Components W and T are also resolved in the H_2O line.
2. The internal kinematics of CO and [C I] 2–1 are clearly dominated by rotation. While the kinematics of the H_2O line in W could be consistent with rotation, the H_2O line in T shows different, disturbed, kinematics.
3. Component T is significantly more extended, in gas and continuum, along its kinematic minor axis, likely the result of spatial magnification due to lensing.
4. Spatially resolved sub-mm SEDs show that component W is well fit with greybody emission from dust at a single temperature over the full extent of the galaxy, but component T requires both an additional component of significantly hotter nuclear dust and additional sources of emission in the mm.

5. We confirm that, in a rough sense, the [C I] 2–1 line can be used as a warm/dense molecular gas tracer in such extreme systems. However, there are several caveats: an excitation temperature assumption is required for [C I] 2–1, the resolved dependence of [C I] 2–1 on CO J:7–6 is slightly flatter than linear, and the morphology of [C I] 2–1 and CO J:7–6 are different in W and T, with the [C I] 2–1 slightly more extended and the CO J:7–6 emission.
6. We obtain an exquisite and unprecedented 2.5 kpc-scale resolved warm/dense gas Schmidt-Kennicutt relationship for components W and T, i.e. an SK relationship in which CO J:7–6 – a tracer of warm/dense gas – is used to trace molecular gas mass spatially. Typical gas exhaustion times for all apertures in W are within 0.5 dex of 1 Gyr; in T the gas exhaustion timescales are about 0.4 dex slower than those in W. Both W and T follow a resolved warm/dense gas SK relationship with power law $n \sim 1.7$, significantly steeper than the $n \sim 1$ found previously, using ‘cold’ (i.e. as traced by, e.g., CO J:1–0) molecular gas, in nearby normal star-forming galaxies.

NN acknowledges funding support from CONICYT CATA/BASAL PFB-06/Etapa II, Fondecyt 1171506 and PIA ACT172033. GO acknowledges the support provided by CONICYT(Chile) through FONDECYT postdoctoral research grant no 3170942. RJI acknowledges support from ERC in the form of Advanced Grant, COSMICISM, 321302.

References

- S. Anderl, V. Guillet, G. Pineau des Forêts, & D. R. Flower, 2013, *A&A* 556, A69
- Bell, E. F., Papovich, C., Wolf, C., et al. 2005, *ApJ*, 625, 23
- Bahé Y. M., Barnes D. J., Dalla Vecchia C., Kay S. T., White S. D. M., McCarthy I. G., Schaye J., Bower R. G. et al. 2017, *MNRAS*, 470, 41864208
- Barnes D. J., Kay S. T., Bahé Y. M., Dalla Vecchia C., McCarthy I. G., Schaye J., Bower R. G., Jenkins A. et al. 2017, *MNRAS*, 471, 1088
- Bekki, K. 2001, *ApJ*, 546, 189
- Benoit Côté, Devin Silvia, Brian W. O’Shea, et al. 2017, arXiv:1710.06442
- Blain et al., 2002, *Physics Reviws*, 369, 111
- Bigiel F., Leroy A., & Walter F., 2008, *AJ*, 136, 2846
- Bigiel F., Leroy, A., Walter, F., et al. 2010, *AJ*, 140, 1194
- Bigiel F. et al., 2011, *ApJL*, 730, L13
- Bisbas, T. G., Papadopoulos, P. P., & Viti, S. 2015, *ApJ*, 803, 37
- Bolatto, A.D., Leroy, A.K., & Wolfire M., 2013, *Annu. Rev. Astron. Astrophys.*, 51:207-68
- Boquien, M., Lisenfeld, U., Duc, P.-A., et al. 2011, *A&A*, 533, A19
- Borne, K. D., Bushouse, H., Lucas, R. A., & Colina, L. 2000, *ApJL*, 529, L77
- Bouché, N., Cresci, G., Davies, R., et al. 2007, *ApJ*, 671, 303
- Bouché, N., Dekel, A., Genzel, R., et al. 2010, *ApJ*, 718, 1001
- Buat, V., Deharveng, J. M., & Donas, J. 1989, *A&A*, 223, 42
- Carilli, C. L., & Walter, F. 2013, *ARA&A*, 51, 105
- Casey, C. M., Narayanan, D., & Cooray, A. 2014, *Phys. Rep.*, 541, 45
- Chabrier, G. 2003, *PASP*, 115, 763
- Chelsea, E., Dominik, A., et al., 2016, *ApJ*, 827, 18
- Cicone, C., Maiolino, R., Sturm, E., et al. 2014, *A&A*, 562, A21
- Daddi, E., Elbaz, D., Walter, F., et al. 2010, *ApJL*, 714, L118
- Davé, R., Finlator, K., & Oppenheimer, B. D. 2012, *MNRAS*, 421, 98
- Davé, R., Oppenheimer, B. D., & Finlator, K. 2011, *MNRAS*, 415, 11
- G. F. Dionne, J. F. Fitzgerald, T-S Chang, M. M. Litvak, and H. R. Fetterman, 1980, *IJIMW*, 1, 4
- Downes D. & Solomon P.M., 1998, *ApJ*, 507, 615
- S. Eales, L. Dunne, D. Clements et al., 2010 *PASP*, 122, 499
- Engel, H., Tacconi, L. J., Davies, R. I., et al. 2010, *ApJ*, 724, 233
- Feruglio, C., Maiolino, R., Piconcelli, E., et al. 2010, *A&A*, 518, L155
- Flower, D. R., & Launay, J. M., 1985, *M.N.R.A.S.*, 214, 271
- Flower, D. R. & Pineau Des Forêts, G. 2010, *MNRAS*, 406, 1745
- Freundlich, J., Combes, F., Tacconi, L. J., et al. 2013, *A&A*, 553, A130
- Fudamoto Y., et al., 2017, *MNRAS*, 000, 1
- Gao, Y. 1997, *PASP*, 109, 1189
- Gao, Y., & Solomon, P. M., 2004, *ApJ*, 606, 271
- Genzel, R., Tacconi, L. J., Gracia-Carpio, J., et al. 2010, *MNRAS*, 407, 2091
- Glenn et al. 2010, *MNRAS*, 409, 109
- Glover, S. C. O., & Clark, P. C. 2016, *MNRAS*, 456, 3596
- Glover, S. C. O., Clark, P. C., Micic, M., & Molina, F. 2015, *MNRAS*, 448, 1607
- Goicoechea, J. R., Chavarría, L., Cernicharo, J., et al. 2015, *ApJ*, 799, 102
- Israel, F. P., Rosenberg, J. F., & van der Werf, P. 2015, *A&A*, 578, A95
- Harris A. I. et al., 2012, *ApJ*, 752, 152
- Hayward et al. 2011, *ApJ*, 743, L22
- Ivion, R. J., Smail, I., Le Borgne, J.-F., et al. 1998, *MNRAS*, 298, 583
- Ivion, R. J., Greve, T. R., Dunlop, J. S., et al. 2007, *MNRAS*, 380, 199
- Ivion, R. J., Papadopoulos, P. P., Smail, I., et al. 2011, *MNRAS*, 412, 1913
- Ivion, R. J., Swinbank, A. M., Smail, I., et al., 2013, *ApJ*, 772, 137 (I13)
- Kennicutt, R. C., Jr. 1989, *ApJ*, 344, 685
- Kennicutt, R. C., Jr. 1998, *ApJ*, 498, 541
- Kennicutt, R. C., Jr., et al. 2007, *ApJ*, 671, 333
- Kennicutt, R. C., Jr & Evans, N. J., II. 2012, *ARAA*, Vol. 50:531-608
- Krajinović et al. 2006
- Krumholz, M. R., & Thompson, T. A. 2007, *ApJ*, 669, 289
- Krumholz, M. R., McKee, C. F., & Tumlinson, J. 2009, *ApJ*, 699, 850
- Liu, T., Kim, K.-T., Yoo, H., et al. 2016, *ApJ*, 829, 59
- Magnelli et al. 2009, *A&A*, 496, 57
- Momose, R., Koda, J., Kennicutt, R. C., Jr., et al. 2013, *ApJ*, 772, L13
- Morton, D. C., & Noreau, L. 1994, *ApJS*, 95, 301
- Müller, H. S. P., Thorwirth, S., Roth, D. A., & Winnewisser, G. 2001, *A&A*, 370, L49
- Lagos, C., Schaye, J., Bahé, Y., Van de Sande, J., Scott, T. K., Barnes B., Timothy A. D., Dalla C. V.,
- Leroy, A. K., Walter, F., Brinks, E., Bigiel, F., de Blok, W. J. G., Madore, B., & Thornley, M. D. 2008, *AJ*, 136, 2782
- Lilly, S. J., Carollo, C. M., Pipino, A., Renzini, A., & Peng, Y. 2013, *ApJ*, 772, 119
- Orellana, G., Nagar, N. M., Elbaz, D., et al. 2017, *A&A*, 602, A68
- Omont, A., Yang, C., Cox, P., et al. 2013, *A&A*, 551, A115
- Oteo, I., Zhang, Z., Yang, C., et al. 2017, arXiv:1701.05901
- Papadopoulos, P. P., Thi, W.-F., & Viti, S. 2004, *MNRAS*, 351, 147
- Popping, G., Decarli, R., Man, A. W. S., et al. 2017, arXiv:1703.05764
- Qian Jiao, Ming Zhu, Nanyao Lu, et al., 2017, *ApJL*, 840, L18
- Rodríguez, M. I., M. Pérez Torres, M. Villar-Martín, et al., 2014, *A&A* 565, A19
- Roychowdhury, S., Huang, M.-L., Kauffmann, G., Wang, J., & Chengalur, J. N. 2015, *MNRAS*, 449, 3700
- Salomé, P., Guélin, M., Downes, D., et al. 2012, *A&A*, 545, A57
- Schartmann, M., Mould, J., Durré, M., et al., 2017, *MNRAS*, 473, 953
- Schmidt, M. 1959, *ApJ*, 129, 243
- Shetty, R., & Ostriker, E. C. 2012, *ApJ*, 754, 2
- Shimajiri, Y., André, P., Braine, J., et al. 2017, *A&A*, 604, A74
- Solomon, P.M., Downes, D., Radford, S.J.E., 1992, *ApJ* 398:L29-L32
- Solomon, P. M., & Sage, L. J. 1988, *ApJ*, 334, 613
- Solomon, P. M., & Vanden Bout, P. A. 2005, *ARA&A*, 43, 677
- Stutzki, J., Graf, U. U., Haas, S., et al. 1997, *ApJ*, 477, L33
- Suková, P., Charzyński, S., & Janiuk, A., 2017, *MNRAS*, 472, 4327
- Thomson, A. P., Ivion, R. J., Owen, F. N., et al. 2015, *MNRAS*, 448, 1874
- van der Werf, P. P., Berciano Alba, A., Spaans, M., et al. 2011, *ApJ*, 741, L38
- Walter, F., Weiß, A., Downes, D., Decarli, R., & Henkel, C. 2011, *ApJ*, 730, 18
- Weiß, A., Henkel, C., Downes, D., & Walter, F. 2003, *A&A*, 409, L41
- Weiß, A., Downes, D., Henkel, C., & Walter, F. 2005, *A&A*, 429, L25
- Wong, T., & Blitz, L. 2002, *ApJ*, 569, 157
- Yang, B., Stancil, P.C., Balakrishnan, N., & Forrey, R.C., 2010, *ApJ*, 718, 1062
- Young, J. S., Schloerb, F. P., Kenney, J. D., & Lord, S. D., 1986, *ApJ*, 304, 443
- Zhang, Z.-Y., Romano, D., Ivion, R. J., Papadopoulos, P. P., & Matteucci, F., 2018, *Nat*, 20180604